



**HAL**  
open science

## Hydrothermal activity along the slow-spreading Lucky Strike ridge segment (Mid-Atlantic Ridge): Distribution, heatflux, and geological controls

J. Escartin, T. Barreyre, M. Cannat, R. Garcia, N. Gracias, A. Deschamps, A. Salocchi, P.-M. Sarradin, V. Ballu

### ► To cite this version:

J. Escartin, T. Barreyre, M. Cannat, R. Garcia, N. Gracias, et al.. Hydrothermal activity along the slow-spreading Lucky Strike ridge segment (Mid-Atlantic Ridge): Distribution, heatflux, and geological controls. *Earth and Planetary Science Letters*, 2015, 431, pp.173-185. 10.1016/j.epsl.2015.09.025 . insu-01244343

**HAL Id: insu-01244343**

**<https://insu.hal.science/insu-01244343v1>**

Submitted on 6 Aug 2020

**HAL** is a multi-disciplinary open access archive for the deposit and dissemination of scientific research documents, whether they are published or not. The documents may come from teaching and research institutions in France or abroad, or from public or private research centers.

L'archive ouverte pluridisciplinaire **HAL**, est destinée au dépôt et à la diffusion de documents scientifiques de niveau recherche, publiés ou non, émanant des établissements d'enseignement et de recherche français ou étrangers, des laboratoires publics ou privés.

1  
2  
3  
4  
5  
6  
7  
8  
9  
10  
11  
12  
13  
14  
15  
16  
17  
18  
19  
20  
21  
22  
23  
24  
25  
26  
27

**Hydrothermal activity along the slow-spreading Lucky Strike ridge segment  
(Mid-Atlantic Ridge): Distribution, heatflux, and geological controls**

J. Escartin<sup>1\*</sup>, T. Barreyre<sup>2</sup>, M. Cannat<sup>1</sup>, R. Garcia<sup>3</sup>, N. Gracias<sup>3</sup>, A. Deschamps<sup>4\*</sup>, A. Salocchi<sup>5</sup>,  
P.-M. Sarradin<sup>6</sup>, and V. Ballu<sup>7</sup>

<sup>1</sup>Laboratoire de Géosciences Marines, IPGP, CNRS UMR7154, Paris, France

<sup>2</sup>Woods Hole Oceanographic Institution, Woods Hole, MA, USA

<sup>3</sup>VICOROB, University of Girona, Spain

<sup>4</sup>Laboratoire Domaines Océaniques, CNRS & Université de Bretagne Occidentale, Brest, France

<sup>5</sup>University of Modena and Reggio Emilia, Modena, Italy

<sup>6</sup>EEP, IFREMER, Brest, France

<sup>7</sup>Université de La Rochelle, La Rochelle, France

\*Corresponding author: Javier Escartin – [escartin.javier@gmail.com](mailto:escartin.javier@gmail.com)

\*Note: This article is dedicated to the memory and contributions of the co-author Anne Deschamps, who passed-away in late 2014 during the preparation and writing of this manuscript.

## 28 **Abstract**

29 We have reviewed available visual information from the seafloor, and recently acquired  
30 microbathymetry for several traverses across the Lucky Strike segment, to evaluate the  
31 distribution of hydrothermal activity. We have identified a new on-axis site with diffuse  
32 flow, Ewan, and an active vent structure ~1.2 km from the axis, Capelinhos. These sites  
33 are minor relative to the Main field, and our total heatflux estimate for all active sites  
34 (200-1200 MW) is only slightly higher than previously published estimates. We also  
35 identify fossil sites W of the main Lucky Strike field. A circular feature ~200 m in  
36 diameter located on the flanks of a rifted off-axis central volcano, is likely a large and  
37 inactive hydrothermal edifice, named Grunnus. We find no indicator of focused  
38 hydrothermal activity elsewhere along the segment, suggesting that the enhanced melt  
39 supply and the associated melt lenses, required to form central volcanoes, also sustain  
40 hydrothermal circulation to form and maintain large and long-lived hydrothermal fields.  
41 Hydrothermal discharge to the seafloor occurs along fault traces, suggesting focusing of  
42 hydrothermal circulation in the shallow crust along permeable fault zones.

43

## 44 **1. Introduction and geological setting**

45 Hydrothermal activity along mid-ocean ridges controls cooling of the oceanic  
46 lithosphere, and impacts its thermal structure and the processes operating there (e.g.,  
47 magmatic emplacement, faulting, seismicity, diking and melt delivery to the seafloor).  
48 Understanding the distribution of hydrothermal activity and its nature is necessary to  
49 quantify the associated heatflux, its partition between diffuse and focus flow  
50 recognizable at the seafloor, and to evaluate the amount of cooling with no expression at  
51 the seafloor (e.g., conductive cooling or low-temperature, diffuse percolation).

52 Slow spreading ridge sections with significant melt supply typically define linear ridge  
53 segments with lengths of a few tens of km to up to ~100 km. These segments typically  
54 develop ridge-parallel normal faults on both flanks, and thick crust at their center  
55 indicating melt-focusing along-axis. As in the case of the Lucky Strike segment, sustained  
56 volcanism may lead to the development of central volcanoes (Escartín et al., 2014). The  
57 slow-spreading Lucky Strike segment is unique in that it has been extensively studied  
58 during more than two decades, following the discovery of the Lucky Strike hydrothermal  
59 field, from hereon referred to as the Main Lucky Strike hydrothermal field (MLSHF),  
60 located at its segment center and at the summit of the central volcano (Langmuir et al.,

61 1997). This is one of the most extensive hydrothermal fields discovered to date, and it is  
62 located along a recent graben dissecting the Lucky Strike central volcano (Humphris et  
63 al., 2002; Ondréas et al., 2009; Barreyre et al., 2012; Escartín et al., 2014). Water-column  
64 studies have also revealed hydrothermal plumes at greater depths than that of the  
65 MLSHF (Wilson et al., 1996; German et al., 1996; Thurnherr et al., 2008). These authors  
66 proposed a yet unidentified source at the southern end of the segment and at a depth of  
67 2000 m.

68 A ~3-3.5 km deep magma chamber (Singh et al., 2006) at the base of a ~600 m thick  
69 Layer 2A (Seher et al., 2010) underlies The MLSHF (Figure 2). Major faults within the rift  
70 valley (Escartín et al., 2014) can be linked to fault reflectors that do not reach the magma  
71 chamber depth in seismic reflection profiles (Combiér et al., 2015). Microseismicity  
72 below the hydrothermal field (Crawford et al., 2013) is unrelated to these fault reflectors,  
73 and likely corresponds to hydrothermal cooling instead (Figure 3).

74 In this paper we provide a synthesis of available information along the Lucky Strike  
75 ridge segment, from seafloor observations and imagery to microbathymetric and  
76 acoustic data (Figure 1). We analyze these data to identify and map new hydrothermal  
77 sites, and use other observables (presence of a magma chamber, microseismicity,  
78 faulting) to constrain the processes controlling distribution and location of hydrothermal  
79 activity along this segment, to re-evaluate heat fluxes at the segment scale, and to  
80 discuss the implications for heat extraction and magmatic supply. Finally, we review  
81 evidence of hydrothermal activity along the segment based on water-column studies.

82

## 83 **2. Data and indicators of hydrothermal activity at the seafloor**

84 The Lucky Strike area has been targeted by numerous cruises in the last 25 years,  
85 providing extensive visual information from direct human observations, video imagery,  
86 and electronic still-camera images acquired with human-operated vehicles (HOVs),  
87 remotely operate vehicles (ROVs), and deep-towed camera systems. These visual  
88 observations are complemented with near-bottom high-resolution bathymetry data  
89 acquired both with ROVs and Autonomous Underwater Vehicles (AUVs) during cruises  
90 in 2008 and 2009, in addition to a prior deep-towed sonar survey (Scheirer et al., 2000;  
91 Humphris et al., 2002; Escartín et al., 2014), as summarized in Figure 1 and  
92 Supplementary Table 1. Near-bottom ROV and AUV bathymetry data have a resolution of  
93 several decimeters to a few meters per pixel, depending on survey altitude, and provide

94 detailed information on the seafloor texture that can be used to discriminate between  
95 hydrothermal structures (e.g., hydrothermal mounds and chimneys, Figure 2) from  
96 other structures whose origin is instead volcanic (e.g., hummocks, lava channels and  
97 flows), tectonic (e.g., faults, fissures), or related to secondary mass-wasting processes  
98 (e.g., landslides along fault scarps).

### 99 *2.1. Visual observations*

100 The bulk of the field work involving visual observations at the seafloor focuses on the  
101 MLSHF, which is yearly visited since 2008 (MoMAR08) and is instrumented for  
102 monitoring since 2010 as part of the MOMARSAT European Multidisciplinary Seafloor  
103 and water column Observatory (EMSO) deep-sea seafloor observatory (Colaço et al.,  
104 2011). In this study we use imagery and visual observations along with HOV, ROV, and  
105 deep-towed camera systems (Figure 1a) that extend both along the Lucky Strike  
106 segment, and across the full rift valley width (Figure 1a), and present a large-area  
107 seafloor photomosaics from vertically-acquired imagery. The first systematic survey of  
108 the MLSHF was conducted with ARGO II towed-camera in 1996 (Humphris et al., 2002;  
109 Escartin et al., 2008). Subsequent surveys conducted with the ROV VICTOR low-light  
110 camera covered fully the MLSHF (Barreyre et al., 2012), extending beyond prior surveys,  
111 and South along the ridge axis (Figure 1). Vertical imagery was processed into a single  
112 georeferenced seamless giga-mosaic. Details on the ARGO II and OTUS image surveys at  
113 MLSHF, and on image processing and mosaicing are provided elsewhere (Escartín et al.,  
114 2008; Barreyre et al., 2012; Prados et al., 2012); here we present for the first time the  
115 2009 photomosaic ~1 km south of the MLSHF.

116 Active hydrothermal sites are readily identifiable visually from venting fluids (high-  
117 temperature black smokers and clear-fluid vents, diffuse outflow at lower temperatures),  
118 hydrothermal macrofauna and microbial communities (e.g., bacterial mats and mussel  
119 beds), or white anhydrite deposits that require venting temperatures of 120-150°C  
120 (Bischoff and Seyfried, 1978). These visual features have been used to extensively map  
121 the MLSHF from both photomosaics and oblique-view imagery acquired with ROVs or  
122 HOVs (Barreyre et al., 2012). Fossil hydrothermal outflow areas are also recognizable by  
123 fossil chimneys, sulfide rubble, and hydrothermal staining, which are clearly  
124 distinguishable from basalt or sediment (Lalou et al., 1989; Barreyre et al., 2012).

125 Supplementary Table 1 and Figure 1 provide an overview of the seafloor visually  
126 explored along >900 km of submersible tracks at the Lucky Strike segment, largely  
127 concentrated at the segment center and the MLSHF. The seafloor photomosaics

128 (Barreyre et al., 2012) image  $\sim 1.5 \text{ km}^2$  of seafloor centered on the MLSHF, and  $\sim 0.4 \text{ km}^2$   
129 on-axis  $\sim 2 \text{ km}$  south of MLSHF. Seafloor observations outside the MLSHF were  
130 conducted primarily during the 1994 DIVA cruise (Fouquet et al., 1994; Ondreas et al.,  
131 1997) with both HOV Nautille and Scampi camera tows to the North, during the 2006  
132 Graviduck cruise (HOV and camera tows), and during ROV dives in subsequent cruises  
133 (Supplementary Table 1). In this paper the visual indicators of hydrothermal activity are  
134 from shipboard observations (cruise reports and published results), and from a  
135 systematic review of ROV and HOV video imagery and seafloor photography available to  
136 us (cruises underlined in Supplementary Table 1).

137

### 138 *2.2. Microbathymetric data*

139 Microbathymetric data acquired in 2006 (MOMARETO cruise, Supplementary Table 1)  
140 (Ondreas et al., 2009), was complemented with MOMAR'08 and Bathyluck'09 surveys  
141 using ROV VICTOR6000 equipped with a RESON 7150 multibeam system, and AUV  
142 Aster-X equipped with a SIMRAD EM2000 multibeam system. After data processing  
143 (ping editing, correction of navigation, filtering, and gridding), the final  
144 microbathymetric grids have a pixel resolution that varies between 25 cm and 2 m per  
145 pixel depending on survey altitude.

146 The MOMAR'08 and Bathyluck'09 surveys were conducted at the segment center and  
147 over the central volcano summit, across the rift valley floor at different locations along  
148 the segment, and at the flank of the southwestern inside corner of the segment end  
149 (Figure 1). The combined set of microbathymetric surveys, which cover  $\sim 35 \text{ km}^2$  of the  
150 Lucky Strike segment seafloor, is one of the most extensive microbathymetry surveys  
151 along a slow-spreading ridge segment, and complements a prior  $\sim 190 \text{ km}^2$  high-  
152 resolution sonar survey (Scheirer et al., 2000a; Escartín et al., 2014). For this study we  
153 analyzed shaded relief and slope maps of the microbathymetric dataset to identify the  
154 seafloor morphology consistent with that of hydrothermal deposits, as described below.

155

### 156 *2.3. Acoustic backscatter data*

157 The central portion of the Lucky Strike segment was surveyed with the DSL120 deep-  
158 towed, near-bottom high-resolution sonar system (Scheirer et al., 2000; Humphris et al.,  
159 2002). These data have been re-processed and presented elsewhere (Escartín et al.,  
160 2014), together with an interpretation of the tectonic and volcanic structure of this

161 portion of the Lucky Strike segment. Sonar data are shifted locally to match the  
162 microbathymetry, as the navigation of the DSL120 towed vehicle is less accurate than  
163 that of ROV or AUVs used in microbathymetric surveys. By themselves sonar data are  
164 not sufficient to identify hydrothermal deposits. First, sulfides do not display acoustic  
165 properties that are distinct from basaltic basemen.. Second, acoustic backscatter  
166 depends on numerous parameters such as insonification direction and angle, acoustic  
167 shading, sedimentation, and instrumental artifacts, among other factors. In this study we  
168 only use acoustic backscatter to support the interpretation of the microbathymetric data.

169

#### 170 *2.4. Identification and extent of hydrothermal sites and fields*

171 Hydrothermal activity with high-temperature fluid discharge ubiquitously displays  
172 mounds and chimneys that can reach up to a few tens of meters above surrounding  
173 seafloor, with basal widths of meters to a few tens of meters (Figure 2). Areas with  
174 hydrothermal vents have a characteristic microbathymetric signature, with spikes and  
175 small-scale lumps, that corresponds to the “lumpy” seafloor morphology described  
176 previously for the MLSHF (Ondreas et al., 2009) (Figure 2a), and for other hydrothermal  
177 fields along mid-ocean ridges (Ferrini et al., 2008; Jamieson et al., 2014) elsewhere  
178 (Figure 2b). This lumpy terrain can be clearly differentiated from the volcanic seafloor  
179 morphology (hummocks, lava flows, lava channels) that tends to be spatially larger  
180 structures (tens to hundreds of m) and that displays instead a smooth seafloor  
181 morphology lacking spikes.

182 Zones with rubble, which are systematically found along slopes of fault scarps or  
183 volcanic structures, show instead a granulated texture due to individual rock blocks,  
184 which are systematically smaller than hydrothermal structures (~1-2 m or less, Figure  
185 2a). This hydrothermal seafloor texture, which is common to hydrothermal fields (e.g.,  
186 Lau Basin, Figure 2b) (Ferrini et al., 2008; Jamieson et al., 2014), is used here to map the  
187 extent of hydrothermal sites within a hydrothermal field, or of new hydrothermal fields.  
188 High-resolution acoustic backscatter, which can reveal this ‘lumpy’ hydrothermal terrain  
189 under optimal insonification conditions, is used to complement the microbathymetry.

190 Imagery (Figure 1a) is critical to confirm that sites identified in the microbathymetry do  
191 correspond to hydrothermal deposits, active or inactive. It is also required to map areas  
192 of diffuse hydrothermal outflow, young hydrothermal activity, or fossil structures, with  
193 no clear morphological signature (bacterial mats, vents, hydrothermal staining, dead

194 chimneys, etc.). Extensive seafloor photomosaics are available for the MLSHF, where the  
195 hydrothermal activity has been extensively mapped (Barreyre et al., 2012), and  
196 additional photomosaics are available for an area ~2 km south of this site, along the  
197 ridge axis (Figure 1a). The rest of the imagery is acquired along HOV, ROV, or tow tracks  
198 (Figure 1a), which is adequate to identify areas of hydrothermal activity but cannot be  
199 used to properly constrain the extent and limits of these areas.

200 Hence, the areas of 'lumpy' hydrothermal terrain identified in this study, based on  
201 microbathymetric data (Figure 1b), indicate zones of significant and sustained  
202 hydrothermal activity with significant sulfide accumulation. The bathymetric data also  
203 reveal numerous volcanic features (hummocks, volcanic cones), tectonic structures  
204 (fault scarps and fissures), and mass wasting indicators (slump scars, debris flows, scree,  
205 dejection cones).

206 Water column studies have also been used to identify hydrothermal activity. High-  
207 temperature black smoker type fluids form buoyant plumes in the water column that  
208 can be detected from turbidity and manganese anomalies (Klinkhammer et al., 1985;  
209 Baker et al., 2001; Baker, 2007; German et al., 2010), while methane anomalies can be  
210 associated with sites showing both high-temperature venting (Lupton, 1990) and low-  
211 temperature serpentinization (Bougault et al., 1993; Charlou and Donval, 1993; Gràcia et  
212 al., 2000). The observations and datasets (microbathymetry, imagery, water column  
213 studies) available along the Lucky Strike segment show thus limitations in the ability to  
214 detect diffuse and very low-temperature outflow or conductive cooling, that are not  
215 associated with either sulfide mounds (Figure 2) or with visual indicators of  
216 hydrothermal activity (bacterial mats, anhydrite and other hydrothermal mineral  
217 deposits).

218

### 219 **3. Hydrothermal sites at the Lucky Strike segment**

220 Based on both the imagery and the microbathymetry shown in Figure 1, we have  
221 characterized the distribution and nature of hydrothermal discharge throughout the rift  
222 valley floor of the Lucky Strike segment. The distribution of hydrothermal activity and  
223 deposits of the Main Lucky Strike hydrothermal field have been mapped in recent  
224 studies (Ondréas et al., 2009; Barreyre et al., 2012). Using the new microbathymetric  
225 data we have identified additional hydrothermal deposits at the western edge of this  
226 main hydrothermal field and extended its limits (Figure 3, Table 1). We also report



227 three additional hydrothermal sites along the Lucky Strike segment (Figure 3). Two out  
228 of these three new sites, Ewan and Capelinhos, have been visited and are confirmed to  
229 be active. The third site at the MLSHF has been visited and confirmed to be inactive (H6;  
230 Figure 4). The fourth site, Grannus, has been identified solely from the microbathymetric  
231 seafloor texture, but lacks direct visual observations to determine if it is active or  
232 inactive, or what may be the nature of the associated hydrothermal deposits.

233

### 234 *3.1. Main Lucky Strike hydrothermal field (MLSHF)*

235 The MLSHF has been systematically mapped and studied during the last two decades  
236 since its discovery in the 90's (Supplementary Table 1) (Langmuir et al., 1997; Humphris  
237 et al., 2002; Escartín et al., 2008; Ondréas et al., 2009; Barreyre et al., 2012; Barreyre et  
238 al., 2014b; Mittelstaedt et al., 2012). Microbathymetry acquired during the Momareto'06  
239 survey has been used to identify the extent, nature, and limits of several areas  
240 corresponding to hydrothermal deposits and associated debris (1 though 4 in Figure 3,  
241 Table 1). This morphological mapping is complemented by large-area seafloor  
242 photomosaics (Escartin et al., 2008; Barreyre et al., 2012; Mittelstaedt et al., 2012;  
243 Prados et al., 2012), used to determine the distribution of both fossil and active venting  
244 (Barreyre et al., 2012) both within these hydrothermal areas and elsewhere throughout  
245 the field (Figure 3).

246 The data collected during the MOMAR'08 and Bathyluck'09 cruises reveal two new  
247 hydrothermal areas at the MLSHF (Areas 5 and 6 in Figure 3). Area 5, which is located in  
248 the southwestern part of the MLSHF and within the axial graben (Figure 3, Table 1), is  
249 associated with zones of diffuse flow and scattered active and inactive vents that are  
250 visible in the microbathymetry.

251 Area 6 is located ~1.5 km from the center axis at the western edge of the MLSHF, and in  
252 the immediate vicinity of the main fault scarp bounding the axial graben. The seafloor in  
253 this area, which corresponds to the flank of an axial volcano recently rifted, is cross-cut  
254 by small-scale normal faults with vertical displacements of up to a few meters, and with  
255 'lumpy' hydrothermal seafloor texture (Figures 3, 4). Area 6a corresponds to a broad  
256 mound with several spikes (vents) extending over an area of ~70x70 m (Figure 4), and  
257 that buries a normal fault scarp that is visible towards the North. Areas 6b and 6c, which  
258 had been previously identified in microbathymetric data (Ondréas et al., 2009), are  
259 smaller and show instead several isolated spikes and no clear mound. Observations from

260 VICTOR#605 dive (MOMARSAT'15 cruise, Figure 4) found no evidence of active  
261 hydrothermal activity, but confirmed that the pinnacles correspond to fossil  
262 hydrothermal chimneys (Figure 4c), and that the area displays numerous indicators of  
263 fossil hydrothermal outflow such as smaller hydrothermal mounds (Figure 4d),  
264 hydrothermal staining, sulfide rubble, shell chaff, and hydrothermal slab similar to that  
265 found at the center of the MLSHF.

### 266 *3.2. Ewan*

267 The Ewan hydrothermal field was serendipitously discovered during HOV Nautilite dive  
268 1624 (Graviluck 2006 cruise, Supplementary Table 1). This dive crossed a series of  
269 seafloor patches covered with filamentous bacterial mats that are white and highly  
270 reflective when illuminated, associated with mussel beds, and primarily found along  
271 scarps and slopes covered with rubble and sediment (Figure 5a-c). Following its  
272 discovery, the site was fully surveyed to obtain seafloor photomosaics and  
273 microbathymetry (Figures 5d-g, MOMAR'08 and Bathyluck'09 cruises, Supplementary  
274 Table 1, Supplementary data). Ewan is located within the axial graben dissecting the  
275 central volcanic cone (Escartín et al., 2014), ~2 km south of the MLSHF (Figures 3 and  
276 5f). The seafloor here displays a complex set of horst and graben (Figure 5f), with  
277 numerous east- and west-verging normal faults that confine the most recent,  
278 unsedimented lava flows (Escartín et al., 2014).

279 In the photomosaics bacterial mats correspond to white areas with a mottled seafloor  
280 aspect (Figures 5c-d), with irregular and gradational limits. Owing to the resolution of  
281 the photomosaics (5-10 mm per pixel), we can also identify macrofauna associated with  
282 the vents (e.g., fish, Figure 5e), but mussel beds associated with the bacterial mats are  
283 not visible in this imagery. Using mapping techniques and interpretation developed  
284 earlier (Barreyre et al., 2012), we identified and digitized ~150 larger patches, in  
285 addition to >400 that are too small to be digitized, and for which we only record their  
286 position. The ~150 digitized patches cover ~275 m<sup>2</sup>, while the rest correspond to ~30  
287 m<sup>2</sup>, attributing 0.06 m<sup>2</sup> to each of the smaller features (~0.25x0.25 m<sup>2</sup>). These estimates  
288 (Table 2) are likely minima as topography is not accounted for (flat projection), and the  
289 photomosaic have gaps where active areas may occur.

290 Ewan contains several clusters of bacterial mats along a NNE-SSW direction, extending  
291 ~250 m along-axis and ~40 m across axis, and in the continuation of aligned pits ~10 m  
292 deep and ~30 m wide (Figure 4g). Bacterial mats occur both along slopes (pits, fault  
293 scarps, Figure 5a-c) and flat-lying, volcanic seafloor (ropy lavas, RL, in Figure 5d).

294 Detailed HOV observations (Figure 3c) revealed shimmering locally, as observed in  
295 diffuse outflow areas at the MLSHF. We did not find active nor fossil high-temperature  
296 venting (e.g., active or fallen chimneys) during the HOV dive or in the seafloor  
297 photomosaics, suggesting that Ewan hosts only diffuse hydrothermal activity. The  
298 distribution and shape of individual bacterial patches also indicates fluid percolation  
299 through the seafloor at very slow flow rates.

300

### 301 *3.3. Capelinhos*

302 Capelinhos is a vent field located ~1.5 km E of the MLSHF, on the western, outward-  
303 dipping flank of a summital volcanic cone (Figures 3 and 6) first identified in the  
304 microbathymetric data (Bathyluck'09 cruise). The site was first visited during an ROV  
305 dive in 2013 (MoMARSAT'13 cruise, Supplementary Table 1), which confirmed its  
306 activity. The microbathymetry shows a main hydrothermal mound that peaks ~20 m  
307 above the surrounding seafloor, centered along the trace of a small fault scarp and  
308 fissure now buried by the hydrothermal deposits (Figure 6d). This hydrothermal edifice,  
309 which links with nearby structures that rise a few meters to 10 m above surrounding  
310 seafloor (Figure 6d), shows a low acoustic backscatter and lacks any clear texture in the  
311 sonar imagery (Figure 6e). ROV dives (Figure 6d) have confirmed the presence of both  
312 inactive and active chimneys with high-temperature outflow through black smokers,  
313 clear vents, and flanges (Figure 6a-c). Visual observations suggest that diffuse flow is  
314 limited at this site, but we lack seafloor photomosaics to accurately evaluate the type,  
315 geometry, and distribution of diffuse flow as done for Ewan and the MLSHF.

316 At a distance of 150 m to the southwest of the Capelinhos vent the bathymetry shows a  
317 ~50 m diameter dome rising ~2-3 m above surrounding seafloor, which has not been  
318 visited to date (Figure 6d). Nearby fissures immediately to the north expose layered  
319 deposits, reminiscent of hyaloclastite layers blanketing the MLSHF (Ondreas et al., 1997;  
320 Ondreas et al., 2009). This structure is located in the immediate vicinity of the fault  
321 buried by Capelinhos, and its associated acoustic backscatter is low and the sonar  
322 featureless, as observed for the main vent structure (Figure 6e). A hydrothermal origin  
323 is inconsistent with its surface morphology, which lacks the typical 'spikes' found in  
324 hydrothermal terrain. Irregular terrain found East of Capelinhos is instead of volcanic  
325 origin (Figures 6d and e). ROV observations in the area show a sedimented seafloor with  
326 pillows visible locally, with no evidence of standing hydrothermal chimneys or mounds,  
327 and possible hydrothermal staining that is local and minor, and that has not been

328 sampled. The associated sonar imagery shows a hummocky volcanic texture that is  
329 common along the axial seafloor of the Mid-Atlantic Ridge (Smith and Cann, 1990; Yeo et  
330 al., 2011).

331

#### 332 *3.4. Grunnus*

333 Microbathymetric data and sonar imagery show a possible off-axis hydrothermal field,  
334 named Grunnus (Figure 7), ~2.5 km west of the MLSHF and corresponding to a  
335 spreading age of ~220 kyrs (Table 1). This structure has a diameter of ~200 m, with  
336 steep flanks, and a platform ~40-50 m above the surrounding seafloor to the S, and that  
337 abuts against the coalescing volcanic cones and hummocks on the flanks of the rifted  
338 central volcano to the north. This platform hosts a 20-m high structure that casts a clear  
339 shadow in the sonar imagery towards the E (Figure 7b). The shape and size of Grunnus  
340 is reminiscent of that of the TAG hydrothermal mound, which has a pancake shape ~200  
341 m in diameter and ~50 m in height (Humphris and Kleinrock, 1996). Microbathymetry  
342 and the sonar data show by small-scale rugosity and pinnacles at its surface that we  
343 attribute to hydrothermal structures (chimneys, mounds). The volcanic mounds to the  
344 north display instead a smooth surface (Figure 7).

345 While the mound at Grunnus has not been visited, we suggest that this off-axis site is  
346 likely inactive. Observations during an HOV dive conducted in 2006 (Graviluck'06 cruise,  
347 Figure 7a) that approached the base of Grunnus yielded no evidence of hydrothermal  
348 deposits, activity, nor indicators of present or past fluid flow. Furthermore, water  
349 column studies nearby (Wilson et al., 1996; Thurnherr et al., 2008) lack a hydrothermal  
350 plume signature, and seismic reflection and refraction data (Singh et al., 2006; Crawford  
351 et al., 2010; Comber et al., 2015) do not image an underlying AMC that may act as a heat  
352 source for an active hydrothermal field.

353 Bathymetry and sonar imagery also show a fault cross-cutting the western flank of the  
354 mound. The fault scarp is well defined and sharp towards the southwest of the mound,  
355 where it shows up to ~5 m of vertical throw and crosscuts seafloor lacking  
356 hydrothermal texture. Across the mound this fault scarp is recognizable but is not as  
357 well-defined, suggesting that deformation postdated mound emplacement and growth.  
358 The difference in fault morphology and height between the mound and surrounding  
359 seafloor may be attributed to the different mode of faulting in poorly consolidated  
360 hydrothermal deposits relative to basaltic seafloor.

361

362

## 363 **4. Discussion**

### 364 *4.1 Magmatic controls on distribution of hydrothermal activity*

365 The review and analysis of seafloor imagery and microbathymetric data along the Lucky  
366 Strike segment (Figure 1) has allowed us to map new areas with fossil hydrothermal  
367 deposits at the western edge of the MLSHF. The location of the four sites at the segment  
368 center, and the lack of any visual or bathymetric indicators of hydrothermal activity  
369 elsewhere along the segment, suggest a link between melt focusing to the segment  
370 center and heat sources stable over long periods of time generating hydrothermal  
371 activity. Our results do not preclude hydrothermal activity elsewhere, that would be  
372 undetected in the absence of visual imagery (diffuse venting with no morphologic  
373 signature), in areas imaged but lacking detailed observations to detect low-temperature  
374 flow that is not associated with bacterial mats or anhydrite deposits, or in areas where  
375 no near-bottom data exists (see section 4.4. for discussion of water column studies).

376 Of the three active fields, MLSHF and Ewan are at the summit of the central volcano,  
377 along the axial graben dissecting it (Ondréas et al., 2009; Escartín et al., 2014), and  
378 immediately above the ~3-3.5 km deep axial magma chamber (AMC) (Singh et al., 2006;  
379 Combiér et al., 2015). The AMC is not centered at the present-day ridge axis, and both  
380 Ewan and MLSHF are located towards its eastern edge, while Capelinhos is located ~700  
381 m east of the AMC's edge (Figure 3 and 8). The AMC also extends ~6 km along-axis,  
382 likely imparting a three-dimensional thermal structure where temperature gradients  
383 can focus flow towards the segment center (Fontaine et al., 2011).

384 The off-axis Grunnus field is on a volcano flank originally emplaced at the Lucky Strike  
385 segment center and since rifted. The original setting is thus similar active on- and near-  
386 axis fields along this segment (MLSHF, Ewan, and Capelinhos, Figure 3). It is likely that,  
387 as in the case of the hydrothermally active segment center, the Grunnus field may have  
388 been animated by a magma chamber underlying the rifted central volcano at the time of  
389 its formation, both now extinct.

390

391

392 *4.2 Faulting, permeability structure, and outflow at the seafloor*

393 Figure 8 presents a schema of fluid flow within the upper crust associated with the  
394 active hydrothermal fields at the active Lucky Strike hydrothermal field, based on  
395 geological observations and geophysical data. First, the permeability of the crust  
396 immediately above the AMC is likely lower than that of the shallow crust Layer 2A  
397 (Barreyre et al., 2014a) owing to its composition and the confining pressure (Figure 8).  
398 This crustal section must host the hydrothermal upwelling animated by the presence of  
399 the AMC, likely to be distributed and in the form of broad hydrothermal plumes of up to  
400 1 km in diameter for reasonable crustal permeabilities (Fontaine et al., 2014), as shown  
401 in Figure 8.

402 Second, fluid flow at the seafloor is not broadly distributed, but localized along or near  
403 faults. This has been well documented for individual vents and areas of diffuse flow  
404 within the MLSHF through detailed hydrothermal and tectonic mapping (Barreyre et al.,  
405 2012), and for the newly discovered active sites. Ewan is set on tectonic depressions  
406 within the axial graben (Figure 5), while the Capelinhos edifice and associated  
407 structures are set at the continuation of fault traces visible in surrounding seafloor  
408 (Figure 6), covered subsequently by hydrothermal deposits. This association between  
409 hydrothermal outflow and faults, widely observed at other deep-sea hydrothermal fields  
410 at all spreading ridges and in different tectonic environments (Kleinrock et al., 1993;  
411 Haymon et al., 2005; Pedersen et al., 2010; Marcon et al., 2013), suggests that permeable  
412 faults channel hydrothermal flow in the shallow crust (Barreyre et al., 2012; Barreyre et  
413 al., 2014a), as illustrated in Figure 8.

414 Rifting and diking at the Lucky Strike segment center have concentrated along the ~1  
415 km-wide axial graben dissecting the Lucky Strike central volcano (Humphris et al., 2002;  
416 Ondréas et al., 2009; Escartín et al., 2014). These processes may play an important role  
417 in the permeability of the crust overlying the AMC, with the development of a zone of  
418 high-permeability following the axial graben, and induced by thermal cracking and  
419 fracturing associated with dike emplacement, and by small-scale faulting that is likely  
420 limited to the shallowest 1-2 km of the crust (Figure 8). An anisotropic permeability  
421 structure, coupled with a magma chamber, can promote along-axis convection cells  
422 (Fontaine et al., 2014) consistent with microseismicity clusters observed here above the  
423 AMC (Crawford et al., 2013), with clusters resulting from cracking-induced  
424 microseismicity induced by cooling. It is thus likely that the two microseismicity clusters  
425 along the axial graben, one immediately north of the MLSHF, and the second below the

426 summit of the axial volcanic cone (Figure 3) correspond to cooling in downflow areas.  
427 Venting at Capelinhos, which is East of the AMC edge, is then likely associated to flow  
428 along a permeable fault that may root at the main upwelling zone and below the Layer  
429 2A (Figure 8). Ewan may correspond instead to a minor axial upwelling relative the  
430 MLSHF, and associated with a downwelling area below the rifted axial volcano located  
431 between these two hydrothermal fields (Figure 3). Alternatively, Ewan may be  
432 associated with a recent magmatic event such as the emplacement of a lava flow or dike  
433 propagation in the shallow crust as suggested by hydrophone data (Dziak et al., 2004).

#### 434 *4.3 Revised hydrothermal heat flux at Lucky Strike*

435 The new observations and results presented here allow us to update the heat flux  
436 estimates of known hydrothermal activity at the Lucky Strike segment (Ewan and  
437 Capelinhos in addition to MLSHF), based on visual and instrumental observations. A  
438 prior estimate of heatflux for MLSHF, based on the photomosaic and a systematic  
439 evaluation of the distribution of vents, yielded values of 195-1086 MW (Barreyre et al.,  
440 2012). As the only new hydrothermal area within this field found in this study is inactive,  
441 this estimate remains unchanged.

442 Ewan displays only diffuse and low-temperature hydrothermal discharge, that we have  
443 fully mapped using the seafloor photomosaics (Figure 5). Adopting the methodology of  
444 Barreyre et al. (2012), we estimate the minimum and maximum heatflux based on the  
445 area of diffuse outflow estimated from the photomosaics (Figure 3), and the estimated  
446 temperature and velocity of the outflow from studies in similar settings (see details in  
447 Barreyre et al., 2012, and Table 2). We obtain a heatflux estimate that ranges from 4.4-  
448 117 MW. In our calculations we likely underestimate the surface of diffuse outflow, as it  
449 is calculated over images projected to a horizontal plane without taking into account the  
450 steep topography present in the area (Figure 5). As in the case of the MLSHF diffuse  
451 fluxes, other uncertainties are the velocity and the temperature of the diffuse outflow,  
452 which are not constrained by systematic measurements at this site. Visual inspection of  
453 the Capelinhos site shows that there are two active main chimneys with a total of ~10-  
454 15 vents identified (Figure 4), in addition to flanges with diffusers. Assuming a total of  
455 10-20 vents with a heatflux of 0.12-0.8 MW/vent (Barreyre et al., 2012; Mittelstaedt et  
456 al., 2012) we estimate the Capelinhos heat-flux at 1.2-16 MW.

457 The hydrothermal heat flux that we estimate for the new active sites (5.6-133 MW, Table  
458 2) are thus minor relative to the 195/1086 MW previously reported for the MLSHF  
459 (Barreyre et al., 2012). This represents an increase of ~10% in our heatflux estimate

460 that is taken up primarily by diffuse hydrothermal outflow (80-90% of the total heatflux,  
461 Table 2), although the importance of diffuse outflow appears to vary greatly from site to  
462 site (100% at Ewan and almost non-existent at Capelinhos).

#### 463 *4.4 Water column anomalies and elusive hydrothermal plumes*

464 Water column studies throughout the Lucky Strike segment report anomalies attributed  
465 to hydrothermal plumes rising from undiscovered fields, although their evidence is  
466 elusive. Light transmission anomalies and elevated CH<sub>4</sub> concentrations south of the  
467 MLSHF and central volcano (Wilson et al., 1996) have been attributed to an unidentified  
468 but large field at ~2100 m (W in Figure 9). During the HEAT cruise (German et al.,  
469 1996), TOBI deep-tow sonar detected one anomaly along the non-transform offset  
470 between Lucky Strike North and Famous segments, and another one at the southern  
471 edge of the nodal basin during a hydrographic cast (G in Figure 9). More recently,  
472 hydrographic stations revealed a water column anomaly at 1800 m bsl at the southern  
473 segment end (Thurnherr et al., 2008) (T in Figure 9). Finally, CH<sub>4</sub> anomalies indicating  
474 low-temperature hydrothermal activity associated with serpentinization and not linked  
475 to black smoker activity (lack of a manganese signature) have been identified at Menez  
476 Hom (Gràcia et al., 2000), and at the southern inside-corner of the Lucky Strike segment  
477 (Gr in Figure 9).

478 Numerous other hydrographic profiles conducted throughout this segment show no  
479 water column anomaly. These including casts during the Gravituck cruise shown in  
480 Figure 9 (Thurnherr et al., 2008), ROV dives during the cruises in 2008 and 2009 (Figure  
481 9 and Supplementary Table 1), or deep-towed surveys using TOBI (German et al., 1996;  
482 Gràcia et al., 1998), which detected no water column anomalies other than those along  
483 the non-transform offset and the end of the segment (German et al., 1996) (Figure 9). In  
484 many casts, the plume of the MLSHF is not detected (Figure 9), likely due to complex  
485 hydrography and strong seafloor currents (Thurnherr et al., 2008) that may sweep or  
486 dilute its plume. Furthermore, seafloor observations and microbathymetry surveys  
487 available in the immediate proximity of some of these anomalies (Figure 9) provide no  
488 evidence of activity away from the three active hydrothermal fields at the center of the  
489 segment (Figure 3). Therefore the evidence for additional undiscovered hydrothermal  
490 fields inferred along the southern portion of the Lucky Strike segment (Wilson et al.,  
491 1996; German et al., 1996; Thurnherr et al., 2008) is weak owing to the unexplained  
492 spatial and temporal inconsistencies of hydrographic data indicating the presence or  
493 absence of hydrothermal plumes, the lack of visual or morphologic indicators of



494 hydrothermal activity away from the segment center, and the complex hydrography of  
495 the area.

#### 496 *4.5. Significance for hydrothermal activity along slow spreading segments*

497 Central volcanoes other than Lucky Strike host active vents. At intermediate-spreading  
498 ridges, Axial Volcano along the Juan de Fuca Ridge is also underlain by a magma  
499 chamber 2.5-3.5 km below seafloor, hosts several hydrothermal sites that are monitored  
500 (Kelley et al., 2014). At slower-spreading ridges, the Menez Gwen field (Ondreas et al.,  
501 1997; Marcon et al., 2013) and the Kobeinsey field (Olafsson et al., 1989) along the Mid-  
502 Atlantic Ridge, and the Soria Moria and Troll Wall along the Arctic Ridges (Pedersen et  
503 al., 2010) all occur on central volcanoes at similar phases of rifting as that of Lucky  
504 Strike, dissected at the summit by narrow and localized axial graben. It is likely that  
505 these sites are also underlain by magma chambers linked to central volcano formation,  
506 and such fields may be common at central volcanoes along ridge segments (Escartín et  
507 al., 2014) that are yet unexplored.

508 Hydrothermal activity at central volcanoes is likely to be persistent over long periods of  
509 time, continuously or intermittently, owing to sustained and enhanced melt supply  
510 required for their formation. This is supported by the presence of both isolated  
511 hydrothermal vents and areas of hydrothermal deposits that are inactive at Lucky Strike  
512 (Area 5, Table 1), and by the off-axis Grunnus site on a rifted central volcano. While  
513 there are no age constraints on hydrothermal deposits at the Main Lucky Strike  
514 hydrothermal field (Figure 3), it likely to have been active over thousands to a few tens  
515 of thousands of years (Humphris et al., 2002; Barreyre et al., 2012). Other basalt-hosted  
516 hydrothermal fields found along axial volcanic ridges (e.g., Broken Spur (Murton et al.,  
517 1994; Murton et al., 1999), Snake Pit (Karson and Brown, 1988), BeeBee (Connelly et al.,  
518 2012) or Lilliput (Haase et al., 2009)) are much smaller in size and probably with  
519 shorter life-spans. These may be likely associated to short-lived heat sources (e.g., dike  
520 intrusions or recent volcanic eruptions). The long-lived hydrothermal fields associated  
521 with central volcanoes are likely to play a major role in the dispersion and propagation  
522 along the ridge-axis of hydrothermal ecosystems and on the biogeography of these  
523 communities (Van Dover et al., 2002).

#### 524 **Conclusions**

525 Extensive seafloor imagery and visual observations together with microbathymetry  
526 acquired with deep-sea vehicles have allowed us to evaluate the distribution of

527 hydrothermal activity at the scale of the Lucky Strike segment, and to re-evaluate the  
528 associated heatflux. The Lucky Strike segment hosts three active hydrothermal fields:  
529 The known MLSHF, Capelinhos, and Ewan. Capelinhos is located 1.3 km E of the axis and  
530 the Main field, and consists of a ~20 m sulfide mound with black smoker vents. Ewan is  
531 located ~1.8 km south from the Main LS field long the axial graben, and displays only  
532 diffuse flow along and around scarps of collapse structures associated with fault scarps.  
533 At the Main Lucky Strike hydrothermal field we have identified an inactive site, thus  
534 broadening the extent of this field. Heat flux estimates from these new sites are  
535 relatively low and correspond to ~10% of the heat flux estimated for the Main field, with  
536 an integrated heatflux of 200-1200 MW. Overall, most of the flux (up to 80-90%) is  
537 associated with diffuse flow, with the Ewan site showing solely diffuse flow and  
538 Capelinhos mostly focused flow. The microbathymetry also reveals a large, off-axis (~2.4  
539 km) hydrothermal field, comparable to the TAG mound in size, on the flanks of a rifted  
540 volcano. The association of these fields to a central volcano, and the absence of  
541 indicators of hydrothermal activity along the ridge segment, suggest that sustained  
542 hydrothermal activity is maintained by the enhanced melt supply and the associated  
543 magma chamber(s) required to build central volcanoes. In all cases hydrothermal  
544 outflow at the seafloor is controlled by faults, indicating that these tectonic structures  
545 are permeable and exploited by the hydrothermal circulation in the shallow crust. Our  
546 observations, together with inconsistencies in available oceanographic data, also fail to  
547 constrain the possible source(s) of all anomalies detected in water column. Central  
548 volcanoes are thus associated with long-lived hydrothermal activity, and these sites may  
549 play a major role in the distribution and biogeography of vent communities.

550

551

552 **Acknowledgements.** This work has been partly financed by ANR (France) Mothseim  
553 Project NT05-3 42213 to JE, by EU-RTN-MOMARNET to MC, and by MINECO (Spain)  
554 project CTM2013-46718-R to RG. The French Ministry of Research financed ship, ROV and  
555 AUV time (Graviluck'06, MOMAR'08, Bathyluck'09, MOMARSAT cruises in 2010-2015).  
556 *TowCam* deployment during Graviluck cruise was supported by NSF grant OCE-0623744 to  
557 A. Soule and D. J. Fornari (WHOI, USA). This is IPGP contribution #3676.

558 **Table 1.** Hydrothermal fields at the Lucky Strike ridge segment. The limit of sites H1 through H4 in the Main Lucky Strike field have been  
 559 defined previously (Ondréas et al., 2009), as well the distribution of focused and diffuse hydrothermal outflow by (Barreyre et al., 2012). Sites  
 560 H5 and H6 in the Main Lucky Strike Field, and the Ewan, Capelinhos, and Grunnus fields are described in this paper.  
 561

<i>Name</i>	<i>Longitude</i>	<i>Latitude</i>	<i>Depth, m</i>	<i>Area, m<sup>2</sup></i>	<i>Distance, km (spreading age, kyr)<sup>#</sup></i>	<i>In situ data</i>	<i>Activity*</i>
<b>Main Lucky Strike field</b>					0-0.6 (0-53)	Visual, photomosaic	
H1	32°16.92'W	37°17.61'N	1620-1720	30304			Active, f+d
H2	32°16.50'W	37°17.48'N	1620-1670	35535			Active, f+d
H3-Eiffel Tower	32°16.52'W	37°17.33'N	1680	1506			Active, f+d
H3a	32°16.60'W	37°17.43'N	1670	5066			Active, f+d
H3b	32°16.62'W	37°17.37'N	1680-1700	3856			Active, f+d
H3c	32°16.52'W	37°17.27'N	1700	1454			Active, f+d
H4	32°16.90'W	37°17.41'N	1710	282			Active, f+d
H5	32°16.84'W	37°17.39'N	1725	10429			Active, f+d
H6a	32°17.08'W	37°17.71'N	1585	4479			Inactive
H6b	32°17.05'W	37°17.64'N	1590	2259			Inactive
H6c	32°17.07'W	37°17.69'N	1590	2597			Inactive
<b>Ewan</b>	32°17.27'W	37°16.61'N	1770	3010	0 (0)	Visual, photomosaic	Active, d
<b>Capelinhos</b>	32°15.83'W	37°17.35'N	1665	20712	1.4 (130)	Visual	Active, f (d)
<b>Grunnus</b>	32°18.25'W	37°18.02'N	1645	35704	2.4 (220)	None	Inactive?

584 Notes: <sup>#</sup>Distance is measured to centerline of axial graben, and spreading age calculated assuming a full spreading rate of 22 km/Myr. For the  
 585 main Lucky Strike we report the minimum and maximum distances and the associated spreading ages.

586 \*Activity of sites is confirmed visually except for Grunnus, which has not been visited to date. Type of flow: f - focused flow (vents); d - diffuse flow.  
 587 Type of flow in parenthesis denotes minor occurrence.

588 **Table 2.** Ranges (min/max)? Heatflux estimates of Lucky Strike hydrothermal fields.  
 589 Calculations are based on the number of high-temperature vents and surface of areas of  
 590 diffuse flow identified visually (this ?study) and instrumental measurements (temperature,  
 591 currents), following the methodology of Barreyre et al. (2012).

592 Ewan hydrothermal field (diffuse)

593 Large patches: S: 274 m<sup>2</sup> Q=4.2/92 MW  
 594 Small matches: Number=1072; S: 11 m<sup>2</sup> Q=0.2/15 MW  
 595 Total EWAN Q=4.4/117 MW

596

597 Capelinhos hydrothermal field (focused)

598 Vents Number= 10-20; Q/vent=0.12-0.8 MW Q=1.2/16 MW

599

600 Main Lucky Strike hydrothermal field (focused + diffuse) (Barreyre et al., 2012)

601 Diffuse flow Q=187/1036 MW  
 602 Focused flow Q=8/50 MW  
 603 Total MLSHF Q=195/1086 MW

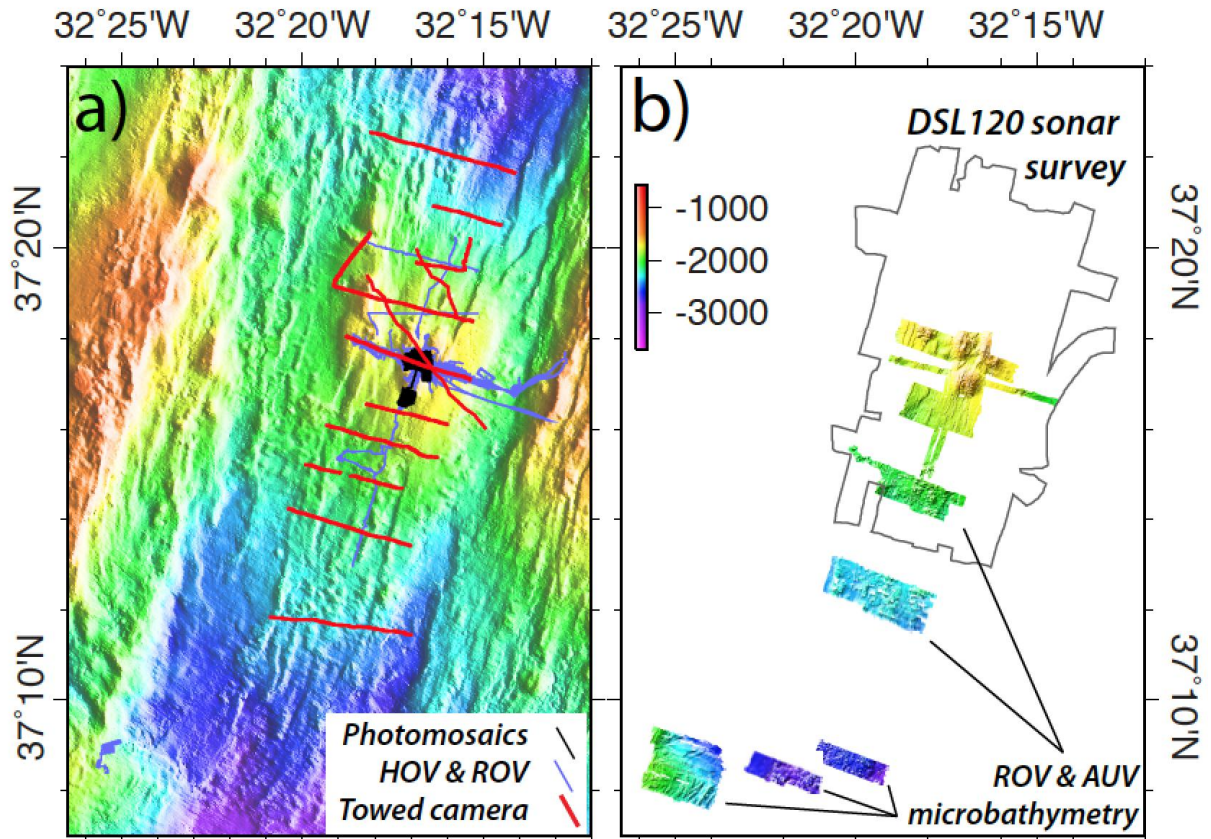
604

605 Combined heat-fluxes at Lucky Strike

606 **Diffuse flow Q=191/1143 MW**  
 607 **Focused flow Q=9/66 MW**  
 608 **Total heatflux Q=200/1210 MW**

609 \* Diffuse flow:  $Q = \Delta T \times \phi \times v \times C_p \times S$ , where  $f$  is density of seawater (1025 kg.m<sup>-3</sup>),  $C_p$  is the  
 610 specific heat of the diffuse fluid (4.2 10<sup>3</sup> J.kg<sup>-1</sup> °C<sup>-1</sup>),  $\Delta T$  is temperature difference  $T-T_0$  between  
 611 outflow temperature  $T$  and ambient seawater  $T_0$  (4.4°C),  $v$  is the diffuse effluent velocity, and  $S$   
 612 the area of considered diffuse outflow (m<sup>2</sup>). T minimum and maximum values are 8 and 20°C,  
 613 and V minimum and maximum values are 1 and 5 mm/s, as described by Barreyre et al. (2012)  
 614 and references therein. S is reported in the Table 1.

615 Focused flow: Individual vent heatflux is estimated at 0.12-8 MW, as described by Barreyre  
 616 et al. (2012). The total heatflux associated to focused flow is the integration of the heatflux from  
 617 individual vents, which are visually identified in available ROV video imagery.

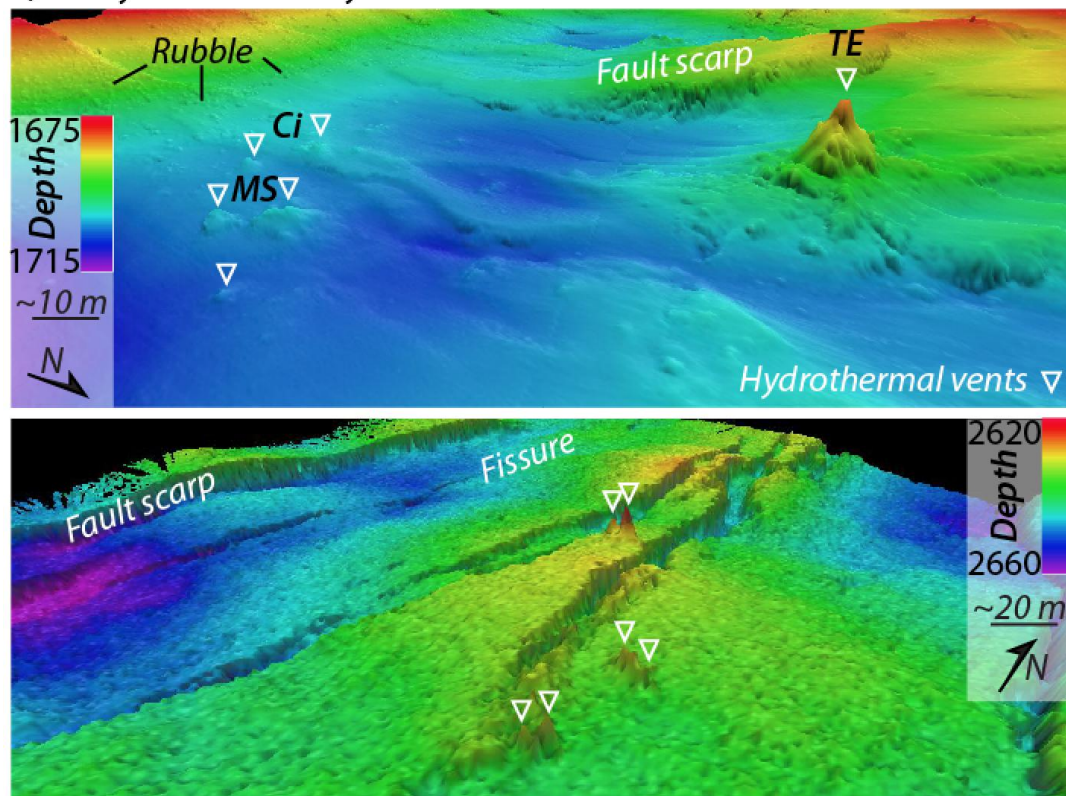


618

619

620 **Figure 1.** a) Visual information of the seafloor is available from ROV photomosaics, and  
 621 along tracks of HOVs, ROVs, and deep-towed cameras. b) Available microbathymetric  
 622 data from the Lucky Strike ridge segment, acquired during near-bottom ROV and AUV  
 623 surveys (Momareto'06 and MOMAR'08 and Bathyluck'09 cruises). The outline of the  
 624 DSL120 sonar survey, acquired during the Lustre'96 cruise, is also shown. See  
 625 Supplementary Table 1 for additional details on these cruises, the deep-sea vehicles  
 626 deployed, and types of data acquired.

a) Lucky Strike Main Hydrothermal Field

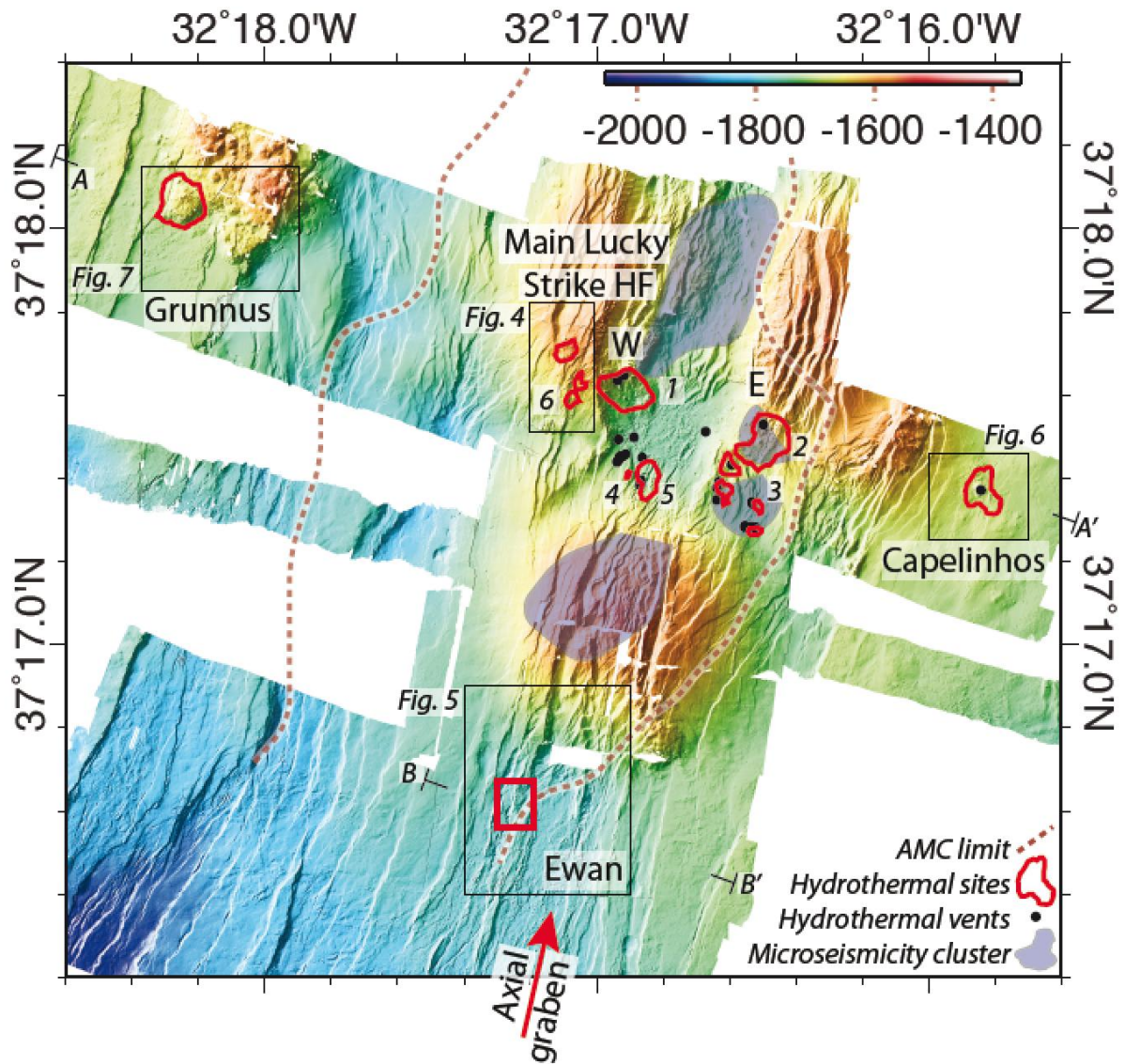


b) Kilo Moana Hydrothermal Field (Lau Basin)

627

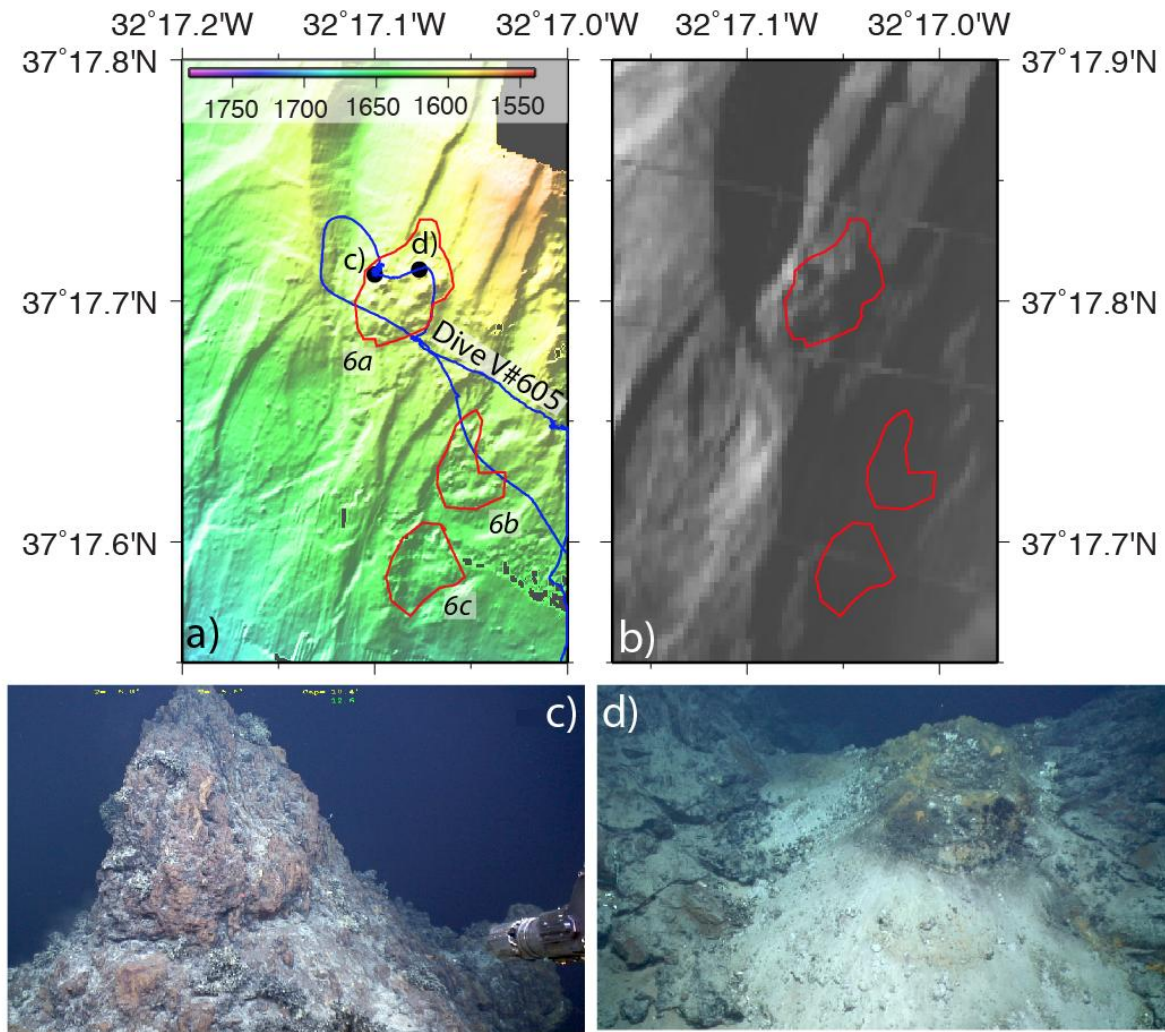
628 **Figure 2.** Perspective views showing the 'lumpy' seafloor morphology associated with  
629 hydrothermal deposits described in the text. a) Microbathymetry from the Lucky Strike  
630 Main Hydrothermal field, showing the ~20 m high Tour Eiffel (TE) vent and the  
631 associated hydrothermal deposits around it, and smaller nearby vents (MS: Montsegur;  
632 Ci: Cimendef). The view shows also several fault scarps and rubble on slopes, that are  
633 morphologically distinct from hydrothermal deposits. b) Microbathymetry showing  
634 hydrothermal vents in the Kilo Moana Hydrothermal Field in the Lau Basin (Ferrini et al.,  
635 2008; Ferrini and Tivey, 2012), rising ~10-20 m above surrounding seafloor that is  
636 faulted and fissured.





637

638 **Figure 3.** Microbathymetry of the Lucky Strike segment center showing the four  
 639 hydrothermal fields identified and the present-day zone of accretion along the axial  
 640 graben (red arrow). Red contours correspond to the limits of hydrothermal deposits  
 641 identified in the microbathymetry, which are numbered for the Main Lucky Strike Field.  
 642 The red square corresponds to the Ewan field, which lacks a geomorphologic signature,  
 643 and black dots correspond to active vents. Boxes indicate the location of Figures 4  
 644 through 7, and characteristics of fields are given in Table 1. The limits of the AMC (Singh  
 645 et al., 2006; Combier et al., 2015) and location of microseismic clusters (Crawford et al.,  
 646 2013) are also shown. A-A' and B-B' indicate endpoints of profiles shown in Figure 8a.



647

648

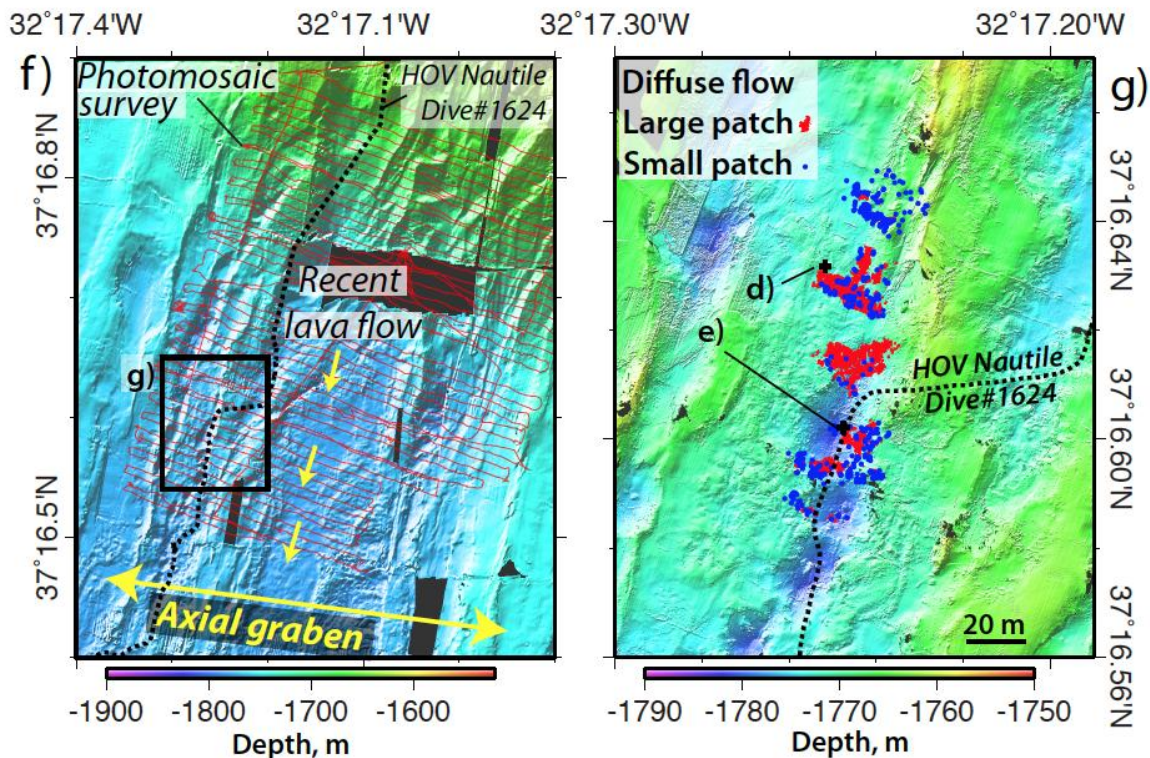
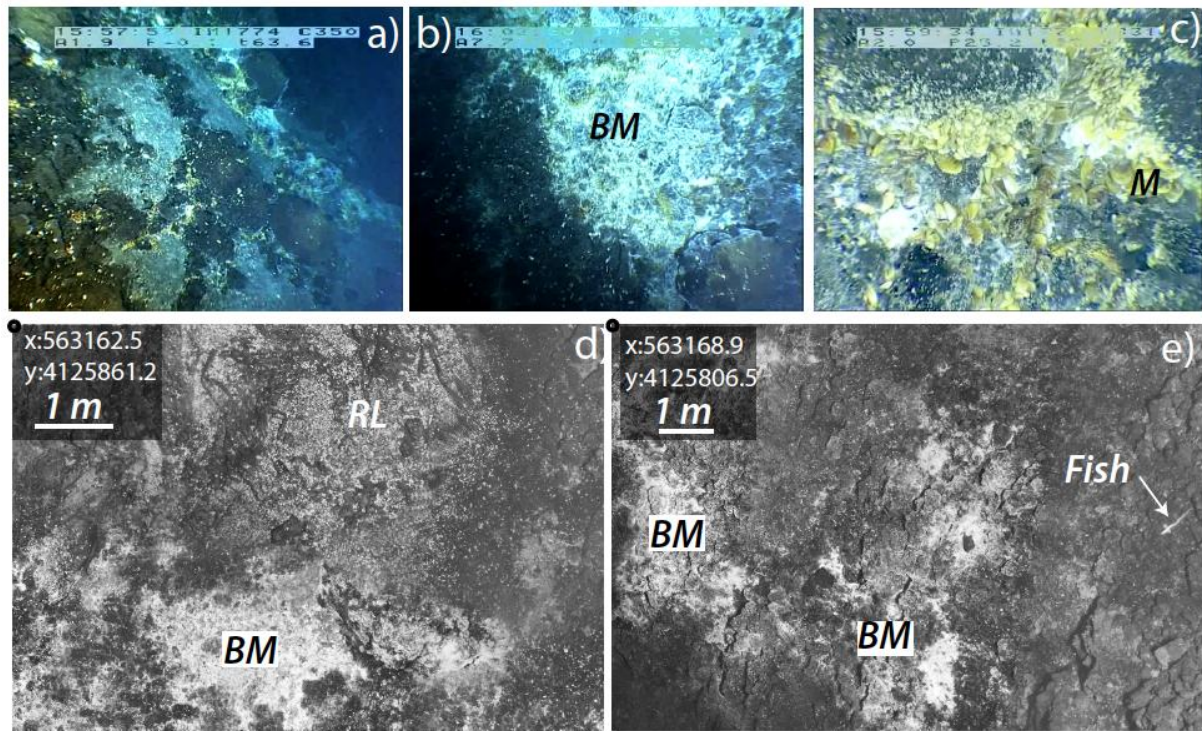
649 **Figure 4.** a) Microbathymetry of the western edge of the MLSHF, showing hydrothermal  
 650 areas 6a-c in red (see Table 1 and Figure 3). c) and d) indicate the location of photos in  
 651 Figures 4c and 4d, respectively. b) Acoustic backscatter image of the same area, with  
 652 insonification from the west. Bright areas correspond to high backscatter, and black to  
 653 acoustic shadows in this and following figures with sonar imagery. c) Inactive chimney  
 654 and d) hydrothermal mound associated deposits observed during ROV VICTOR dive  
 655 #605 (blue line).

656

657

658

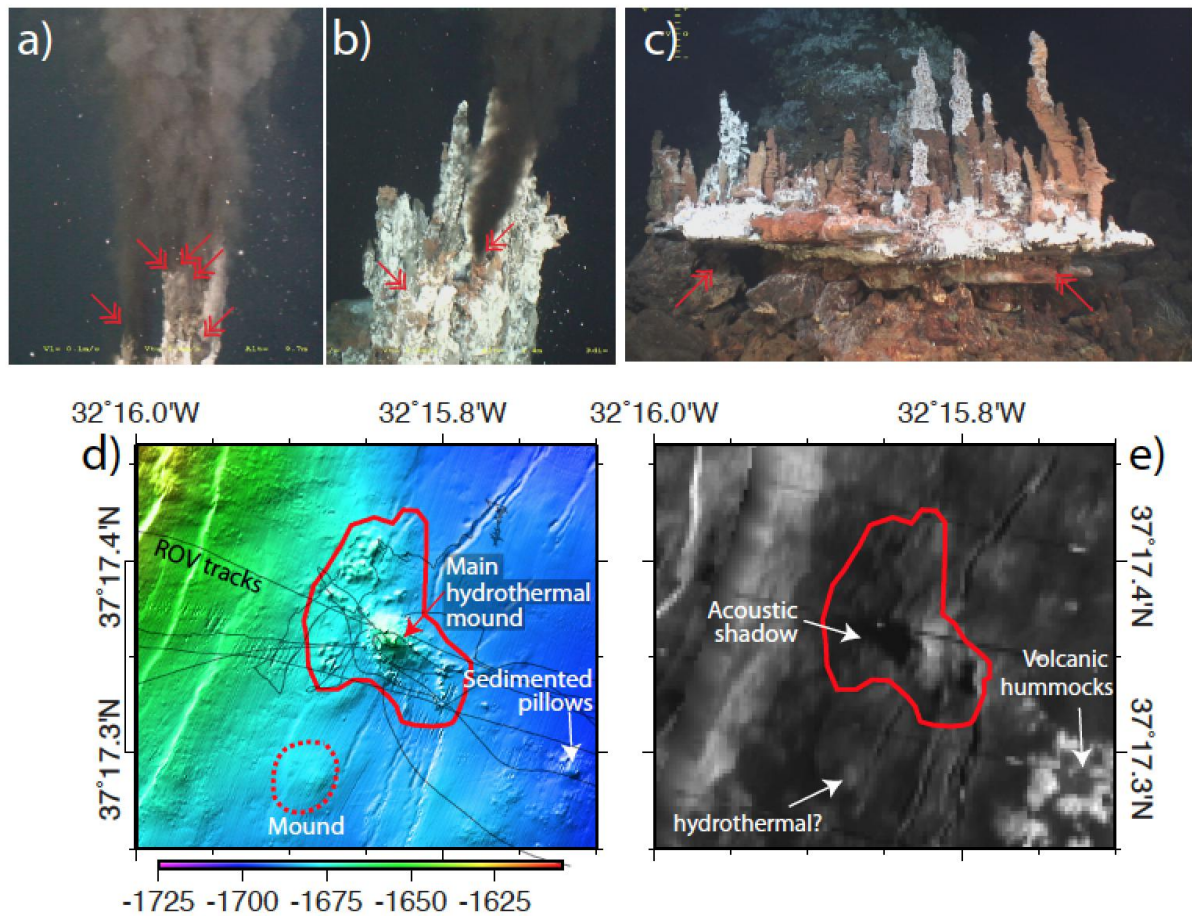




659

660 **Figure 5.** Ewan hydrothermal field. a)-c) Video grabs from HOV Nautilé dive #1616  
 661 (Graviluck'06) show hydrothermal activity along steep slopes (a), with irregular patches  
 662 of bacterial mats and diffuse flow through rubble (b), and associated with mussel beds  
 663 (c). d) Vertical seafloor image mosaics (Bathyluck'09) showing patches of bacterial mats  
 664 (BM) associated with diffuse flow extending over several meters over sedimented ropy  
 665 lava flows (RL). e) Irregular bacterial mat patches, indicating localized diffuse outflow  
 666 through steep scarps. Microbathymetry (50 cm/pixel) of the ridge axis on the southern  
 667 flank of the rifted seamount south of the Main Lucky Strike field (f) and detail of the  
 668 active zones (g). The coordinates of the top left corner of the photomosaics d) and e) are  
 669 in UTM (m), and located in g). See Supplementary Data for photomosaic of this area and  
 670 digitized zones of hydrothermal outflow.

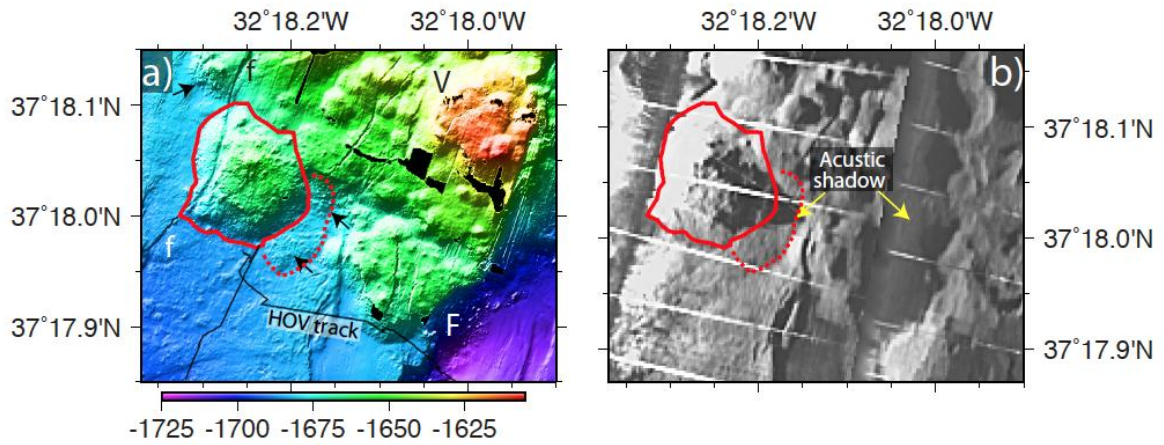




672

673 **Figure 6.** Capelinhos hydrothermal site. The main Capelinhos hydrothermal mound  
 674 shows active chimneys with several black smoker vents (a-b) flanges with diffusers (c).  
 675 Diffuse hydrothermal activity (bacterial mats) is scarce. d) Microbathymetry of the  
 676 Capelinhos hydrothermal field (red outline), which displays a ~20 m high edifice  
 677 emplaced over a set of small-scale faults and fissures, and a possible hydrothermal  
 678 mound to the south (not visually inspected). e) Acoustic backscatter image with  
 679 insonification from the E, showing the acoustic shadow of the edifice. The bathymetry  
 680 reveals several mounds in surrounding areas (arrows); the structure to the SW has low  
 681 acoustic backscatter and may correspond to another hydrothermal deposit. The  
 682 structures to the SE are instead acoustically reflective and the sonar texture corresponds  
 683 to volcanic hummocks.

684

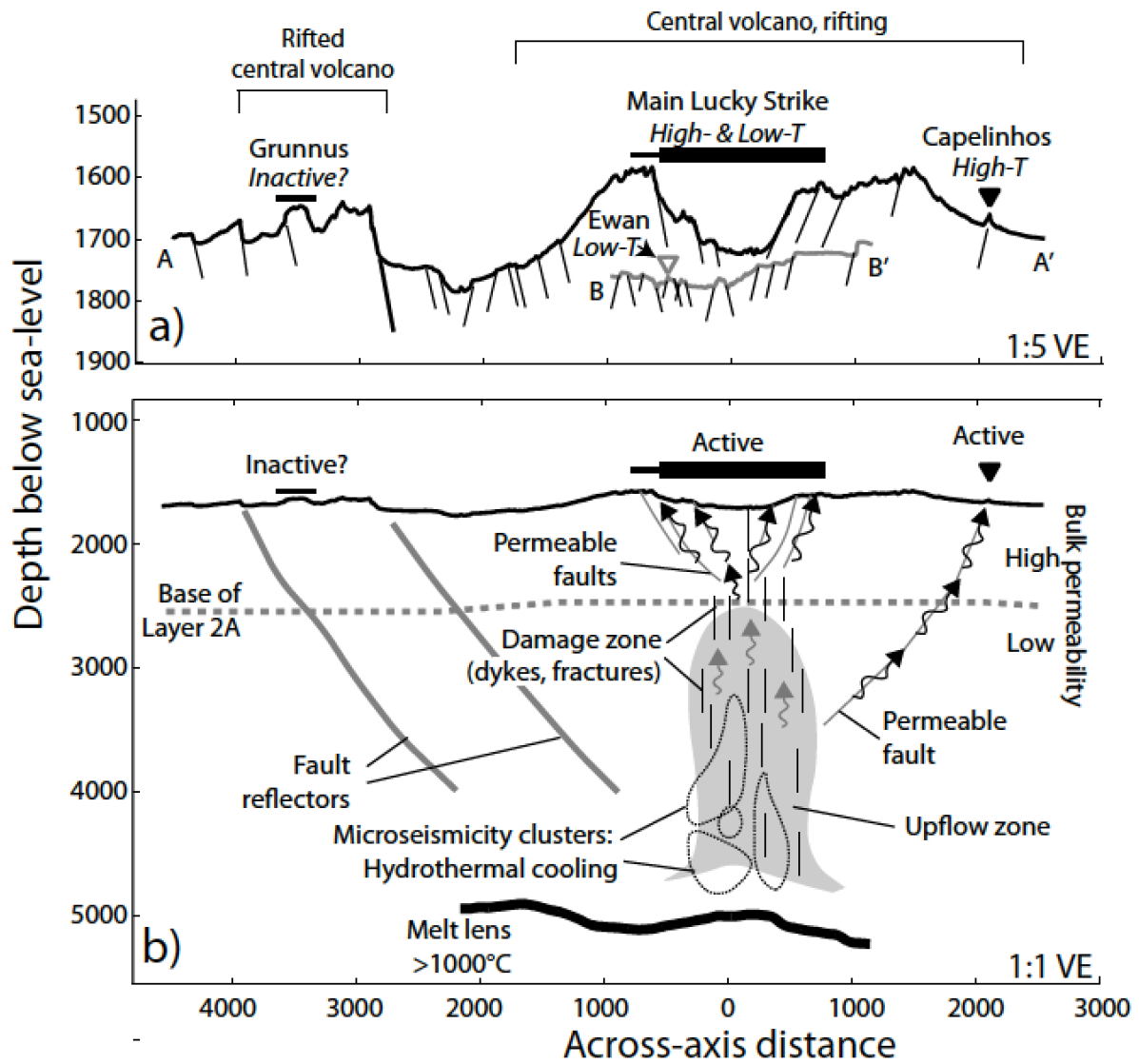


685

686

687 **Figure 7.** a) Microbathymetry of the Grunnus hydrothermal field (solid red line), and  
 688 other possible hydrothermal structures (black arrows, dashed red line) located on the  
 689 flank of a rifted central volcano (V, see Figure 3). A small normal fault (f) dissects the  
 690 western flank of the ~200 meter diameter mound, while major fault (F) that dissects the  
 691 central volcano can be linked to a fault seismic reflector to a depth of ~2 km below  
 692 seafloor (Smith et al., 2006; Combi et al., 2015). b) Corresponding sonar imagery of the  
 693 area.

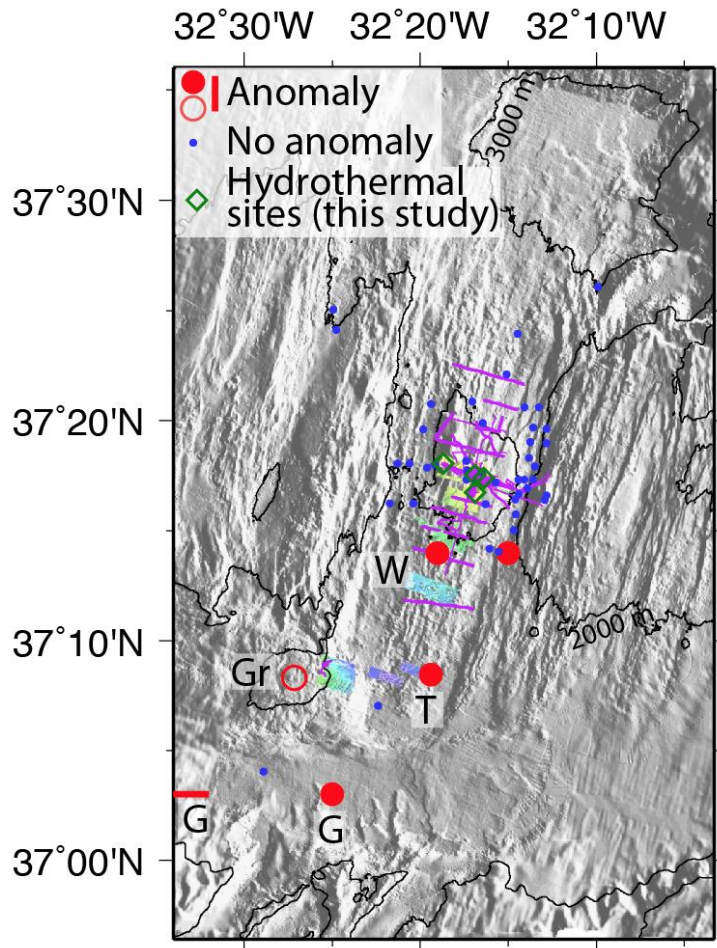
694



695

696 **Figure 8.** a) Microbathymetric profiles across the Grunnus-MLSHF-Capelinhos (black  
 697 line) and across Ewan (grey line, see Figure 3 for location). b) Vertical cross-axis  
 698 section of the crust showing the AMC and fault reflectors (Singh et al., 2006; Comber et  
 699 al., 2015) and the base of Layer 2A (Seher et al., 2010) from seismic data, and the  
 700 projected positions of microseismicity clusters (Crawford et al., 2013). Hydrothermal  
 701 upflow below Layer 2A is likely diffuse in the form of upwellings up to ~1 km in  
 702 diameter (Fontaine et al., 2014) along the axis, which has a higher permeability due to  
 703 damage induced by diking and cracking (Fontaine et al., 2014; Escartín et al., 2014). In  
 704 the shallow crust hydrothermal outflow is likely channeled instead along permeable  
 705 faults.

706



707

708 **Figure 9.** Map of the Lucky Strike field showing the location of water column  
 709 nephelometry anomalies interpreted as indicators of hydrothermal plumes at depths of  
 710 ~1800 m bsl (red), and hydrographic casts conducted during the Graviduck2006 cruise  
 711 that yielded no anomalies (blue). Shaded relief is from shipboard bathymetry, the  
 712 purple lines correspond to visual seafloor observations (Figure 1), the AUV and ROV  
 713 microbathymetry is shown in color (see Figure 3), and sites described in this paper  
 714 indicated by green diamonds. Water column anomalies: G: (German et al., 2006); T  
 715 (Thurnherr et al., 2008); W (Wilson et al., 1996); Gr (Gràcia et al., 2000).

716 **References**

- 717 Baker, E.T., 2007, Hydrothermal cooling of mid ocean ridge axes: Do measured and  
718 modeled heat fluxes agree? *Earth and Planetary Science Letters*, v. 263, p. 140–150.
- 719 Baker, E.T., Cormier, M.-H., Langmuir, C.H., and Zavala, K., 2001, Hydrothermal plumes  
720 along segments of contrasting magmatic influence, 15°20'–18°30'N, East Pacific  
721 Rise; Influence of axial faulting: *Geochemistry, Geophysics, Geosystems*, v. 2, p.  
722 2000GC000165.
- 723 Barreyre, T., Escartín, J., Garcia, R., Cannat, M., Mittelstaedt, E., and Prados, R., 2012,  
724 Structure, temporal evolution, and heat flux estimates from the Lucky Strike deep-  
725 sea hydrothermal field derived from seafloor image mosaics: *Geochemistry,*  
726 *Geophysics, Geosystems*, v. 13, no. 4, p. Q04007, doi: 10.1029/2011GC003990.
- 727 Barreyre, T., Escartin, J., Sohn, R., and Cannat, M., 2014a, Permeability of the Lucky Strike  
728 deep-sea hydrothermal system: Constraints from the poroelastic response to ocean  
729 tidal loading: *Earth and Planetary Science Letters*, v. 408, p. 146–154, doi:  
730 10.1016/j.epsl.2014.09.049.
- 731 Barreyre, T., Escartín, J., Sohn, R.A., Cannat, M., Ballu, V., and Crawford, W.C., 2014b,  
732 Temporal variability and tidal modulation of hydrothermal exit-fluid temperatures  
733 at the Lucky Strike deep-sea vent field, Mid-Atlantic Ridge: *Journal of Geophysical*  
734 *Research: Solid Earth*, v. 119, no. 4, p. 2543–2566, doi: 10.1002/2013JB010478.
- 735 Bischoff, J.L., and Seyfried, W.E., 1978, Hydrothermal chemistry of seawater from 25° to  
736 350°C: *American Journal of Science*, v. 278, p. 838–860.
- 737 Bougault, H., Charlow, J.-L., Fouquet, Y., Needham, H.D., Vaslet, N., Appriou, P., Jean  
738 Baptiste, P., Rona, P.A., Dmitriev, L., and Silantiev, S., 1993, Fast and slow-spreading  
739 ridges: Structure and hydrothermal activity, ultramaphic topographic highs, and  
740 CH<sub>4</sub> output: *Journal of Geophysical Research*, v. 98, no. B6, p. 9643–9651.
- 741 Charlou, J.-L., and Donval, J.-P., 1993, Hydrothermal methane venting between 12°N and  
742 26°N along the Mid-Atlantic ridge: *Journal of Geophysical Research*, v. 98, no. B6, p.  
743 9625–9642.
- 744 Colaço, A., Blandin, J., Cannat, M., Carval, T., Chavagnac, V., Connelly, D., Fabian, M.,  
745 Ghiron, S., Goslin, J., Miranda, J.M., Reverdin, G., Sarrazin, J., Waldmann, C., and  
746 Sarradin, P.-M., 2011, MoMAR-D: a technological challenge to monitor the dynamics  
747 of the Lucky Strike vent ecosystem: *ICES Journal of Marine Science*, v. 68, no. 2, p.  
748 416–424. doi:10.1093/icesjms/fsq075.
- 749 Combier, V., Seher, T., Singh, S.C., Crawford, W.C., Cannat, M., Escartín, J., and Dusunur, D.,  
750 2015, Three-dimensional geometry of axial magma chamber roof and faults at  
751 Lucky Strike volcano on the Mid-Atlantic Ridge: *Journal of Geophysical Research:*  
752 *Solid Earth*, p. n/a–n/a, doi: 10.1002/2015JB012365.
- 753 Connelly, D.P., Copley, J.T., Murton, B.J., Stansfield, K., Tyler, P. a, German, C.R., Van Dover,  
754 C.L., Amon, D., Furlong, M., Grindlay, N., Hayman, N., Hühnerbach, V., Judge, M., Le  
755 Bas, T., et al., 2012, Hydrothermal vent fields and chemosynthetic biota on the  
756 world's deepest seafloor spreading centre.: *Nature communications*, v. 3, p. 620,  
757 doi: 10.1038/ncomms1636.



- 758 Crawford, W.C., Rai, A., Singh, S.C., Cannat, M., Escartín, J., Wang, H., Daniel, R., and  
759 Combier, V., 2013, Hydrothermal seismicity beneath the summit of Lucky Strike  
760 volcano, Mid-Atlantic Ridge: *Earth and Planetary Science Letters*, v. 373, p. 118–  
761 128.
- 762 Crawford, W.C., Singh, S.C., Seher, T., Combier, V., Dusunur, D., Cannat, M., Rona, P.,  
763 Devey, C.W., Dymont, J., and Murton, B., 2010, Crustal structure, magma chamber  
764 and faulting beneath the Lucky Strike hydrothermal fields, *in* Diversity of  
765 Hydrothermal Systems on Slow Spreading Ocean Ridges, AGU, Washington DC, p.  
766 113–132.
- 767 Van Dover, C.L., German, C.R., Speer, K.G., Parson, L.M., and Vrijenhoek, R.C., 2002,  
768 Evolution and Biogeography of Deep-Sea Vent and Seep Invertebrates: *Science*, v.  
769 295, p. 1253–1257.
- 770 Dziak, R.P., Smith, D.K., Bohnenstiehl, D.R., Fox, C.G., Desbruyères, D., Matsumoto, H.,  
771 Tolstoy, M., and Fornari, D.J., 2004, Evidence of a recent magma dike intrusion at the  
772 slow spreading Lucky Strike segment, Mid-Atlantic Ridge: *Journal of Geophysical*  
773 *Research*, v. 109, p. B12102, doi: 10.1029/2004JB003141.
- 774 Escartín, J., García, R., Delaunoy, O., Ferrer, J., Gracias, N., Elibol, A., Cufi, X., Fornari, D.J.,  
775 Humphris, S.E., and Renard, J., 2008, Globally-aligned photo mosaic of the Lucky  
776 Strike hydrothermal Vent Field (Mid-Atlantic Ridge, 37°18.5'N): release of geo-  
777 referenced data, mosaic construction and viewing software: *Geochemistry,*  
778 *Geophysics, Geosystems*, v. 9, no. 12, p. Q12009, doi:10.1029/2008GC002204.
- 779 Escartin, J., Garcia, R., Delaunoy, O., Ferrer, J., Gracias, N., Elibol, A., Cufi, X., Neumann, L.,  
780 Fornari, D.J., Humphris, S.E., and Renard, J., 2008, Globally aligned photomosaic of  
781 the Lucky Strike hydrothermal vent field (Mid-Atlantic Ridge, 37 degrees 18.50 ` N):  
782 Release of georeferenced data, mosaic construction, and viewing software:  
783 GEOCHEMISTRY GEOPHYSICS GEOSYSTEMS, v. 9, doi: 10.1029/2008GC002204.
- 784 Escartín, J., Soule, S.A., Cannat, M., Fornari, D.J., Düşünür, D., and Garcia, R., 2014, Lucky  
785 Strike seamount: Implications for the emplacement and rifting of segment-centered  
786 volcanoes at slow spreading mid-ocean ridges: *Geochemistry, Geophysics,*  
787 *Geosystems*, v. 15, no. 11, p. 4157–4179, doi: 10.1002/2014GC005477.
- 788 Ferrini, V., and Tivey, M.K., 2012, ROV Jason 2 near-bottom multibeam bathymetry grids  
789 from 6 vent fields in the Lau Back-arc Basin: *Integrated Earth Data Applications*  
790 (IEDA), p. <http://doi.org/10.1594/IEDA/100028>.
- 791 Ferrini, V.L., Tivey, M.A., Carbotte, S.M., Martinez, F., and Roman, C., 2008, Variable  
792 morphologic expression of volcanic, tectonic, and hydrothermal processes at six  
793 hydrothermal vent fields in the Lau back-arc basin: *Geochemistry, Geophysics,*  
794 *Geosystems*, v. 9, no. 7, p. Q07022, doi:10.1029/2008GC002047.
- 795 Fontaine, F.J., Cannat, M., Escartin, J., and Crawford, W.C., 2014, Along-axis hydrothermal  
796 flow at the axis of slow spreading Mid-Ocean Ridges: Insights from numerical  
797 models of the Lucky Strike vent field (MAR): *Geochemistry, Geophysics,*  
798 *Geosystems*, v. 15, no. 7, p. 2918–2931, doi: 10.1002/2014GC005372.
- 799 Fontaine, F.J., Olive, J.A., Cannat, M., Escartin, J., and Perol, T., 2011,  
800 Hydrothermally-induced melt lens cooling and segmentation along the axis of fast-

- 801 and intermediate-spreading centers: *Geophysical Research Letters*, v. 38, p. L14307,  
802 doi:10.1029/2011GL047798.
- 803 Fouquet, Y., Charlou, J.L., Costa, I., Donval, J.P., Radford-Knoery, J., Pellé, H., Ondréas, H.,  
804 Lourenço, N., Ségonzac, M., and Tivey, M.K., 1994, A detailed study of the Lucky  
805 Strike hydrothermal site and discovery of a new hydrothermal site: Menez Gwen;  
806 Preliminary results of the DIVAI Cruise (5-29 May, 1994): *InterRidge News*, v. 3, no.  
807 2, p. 14–17.
- 808 German, C.R., Baker, E.T., Connelly, D.P., Lupton, J.E., Resing, J., Prien, R.D., Walker, S.L.,  
809 Edmonds, H.N., and Langmuir, C., 2006, Hydrothermal exploration of the Fonualei  
810 Rift and Spreading center and the Northeast Lau spreading center: *Geochemistry,*  
811 *Geophysics, Geosystems*, v. 7, no. 11, p. Q11022, doi:10.1029/2006GC001324.
- 812 German, C.R., Parson, L.M., and Team, H.S., 1996, Hydrothermal exploration near the  
813 Azores Triple Junction: tectonic control of venting at slow-spreading ridges: *Earth*  
814 *and Planetary Science Letters*, v. 138, p. 93–104.
- 815 German, C.R., Thurnherr, A.M., Knoery, J., Charlou, J.L., Jean Baptiste, P., and Edmonds,  
816 H.N., 2010, Heat, volume and chemical fluxes from submarine venting: A synthesis  
817 of results from the Rainbow hydrothermal field, 361N MAR: *Deep-Sea Research I*, v.  
818 57, p. 518–527.
- 819 Gràcia, E., Charlou, J.L., Radford-Knoery, J.R., and Parson, L.M., 2000, Non-transform  
820 offsets along the Mid-Atlantic Ridge south of the Azores (38°N–34°N): Ultramafic  
821 exposures and hosting of hydrothermal vents: *Earth and Planetary Science Letters*,  
822 v. 177, p. 89–103.
- 823 Gràcia, E., Parson, L.M., Bideau, D., and Hekinian, R., 1998, Volcano-tectonic variability  
824 along segments of the Mid-Atlantic Ridge between the Azores platform and Hayes  
825 fracture zone: Evidence from submersible and high-resolution side-scan sonar data,  
826 *in* Mills, R.A. and Harrison, K. eds., *Modern ocean floor processes and the geological*  
827 *record*, Geological Society, London, p. 1–15.
- 828 Haase, K.M., Koschinsky, A., Petersen, T., Devey, C.W., German, C., Lackschewitz, K.S.,  
829 Melchert, B., Seifert, R., Borowski, C., Giere, O., and Paulick, H., 2009, Diking, young  
830 volcanism and diffuse hydrothermal activity on the southern Mid-Atlantic Ridge:  
831 The Lilliput field at 9°33'S: *Marine Geology*, v. 266, p. 52–64.
- 832 Haymon, R.M., Macdonald, K.C., Benjamin, S.B., and Ehrhardt, C.J., 2005, Manifestations of  
833 hydrothermal discharge from young abyssal hills on the fast-spreading East Pacific  
834 Rise flank: *Geology*, v. 33, p. 153–156; doi: 10.1130/G21058.1.
- 835 Humphris, S.E., Fornari, D.J., Scheirer, D.S., German, C.R., and Parson, L.M., 2002,  
836 Geotectonic setting of hydrothermal activity on the summit of Lucky Strike  
837 seamount (37°17'N, Mid-Atlantic Ridge): *Geochemistry, Geophysics, Geosystems*, v.  
838 3, no. 8, p. 10.1029/2001GC000284.
- 839 Humphris, S.E., and Kleinrock, M.C., 1996, Detailed morphology of the TAG active  
840 hydrothermal mound: Insights into its formation and growth: *Geophysical Research*  
841 *Letters*, v. 23, no. 23, p. 3443–3446.



- 842 Jamieson, J.W., Clague, D. a., and Hannington, M.D., 2014, Hydrothermal sulfide  
843 accumulation along the Endeavour Segment, Juan de Fuca Ridge: *Earth and*  
844 *Planetary Science Letters*, v. 395, p. 136–148, doi: 10.1016/j.epsl.2014.03.035.
- 845 Karson, J.A., and Brown, J.R., 1988, Geologic setting of the Snake Pit hydrothermal site:  
846 an active vent field on the Mid-Atlantic Ridge: *Marine Geophysical Researches*, v. 10,  
847 p. 91–107.
- 848 Kelley, D.S., Delaney, J.R., and Juniper, S.K., 2014, Establishing a new era of submarine  
849 volcanic observatories: Cabling Axial Seamount and the Endeavour Segment of the  
850 Juan de Fuca Ridge: *Marine Geology*, v. 352, p. 426–450, doi:  
851 10.1016/j.margeo.2014.03.010.
- 852 Kleinrock, M.C., Humphris, S., and Thompson, G., 1993, Relations between volcanism,  
853 tectonism and hydrothermalism along the TAG segment of the Mid-Atlantic ridge:  
854 WHOI.
- 855 Klinkhammer, G., Rona, P., Greaves, M., and Elderfield, H., 1985, Hydrothermal  
856 manganese plumes in the Mid-Atlantic Ridge rift valley: *Nature*, v. 314, p. 727–731.
- 857 Lalou, C., Brichet, E., and Lange, J., 1989, Fossil hydrothermal sulfide deposits at the  
858 Galapagos Spreading Centre near 85°00 West: geological setting, mineralogy and  
859 chronology: *Oceanologica acta*, v. 12, no. 1, p. 1–8.
- 860 Langmuir, C., Humphris, S., Fornari, D., Van Dover, C., Von Damm, K., Tivey, M.K.,  
861 Colodner, D., Charlou, J. -l., Desonie, D., Wilson, C., Fouquet, Y., Klinkhammer, G., and  
862 Bougault, H., 1997, Hydrothermal vents near a mantle hot spot: the Lucky Strike  
863 vent field at 37°N on the Mid-Atlantic Ridge: *Earth and Planetary Science Letters*, v.  
864 148, p. 69–91.
- 865 Lupton, J., 1990, Water column hydrothermal plumes on the Juan de Fuca Ridge: *Journal*  
866 *of Geophysical Research*, v. 95, no. B8, p. 12829–12842.
- 867 Marcon, Y., Sahling, H., Borowski, C., dos Santos Ferreira, C., Thal, J., and Bohrmann, G.,  
868 2013, Megafaunal distribution and assessment of total methane and sulfide  
869 consumption by mussel beds at Menez Gwen hydrothermal vent, based on geo-  
870 referenced photomosaics: *Deep Sea Research Part I: Oceanographic Research*  
871 *Papers*, v. 75, p. 93–109, doi: 10.1016/j.dsr.2013.01.008.
- 872 Mittelstaedt, E., Escartín, J., Gracias, N., Olive, J.-A., Barreyre, T., Davaille, A., Cannat, M.,  
873 and Garcia, R., 2012, Quantifying diffuse and discrete venting at the Tour Eiffel vent  
874 site, Lucky Strike hydrothermal field: *Geochemistry Geophysics Geosystems*, v. 13,  
875 no. 4, p. Q04008, doi: 10.1029/2011GC003991.
- 876 Murton, B.J., Klinkhammer, G., Becker, K., Briais, A., Edge, D., Hayward, N., Millard, N.,  
877 Mitchell, I., Rousse, I., Rudnicki, J.W., Sayanagi, K., Sloan, H., and Parson, L., 1994,  
878 Direct evicence for the distribution and occurrence of hydrothermal activity  
879 between 27°N -30°N on the Mid-Atlantic Ridge: *Earth and Planetary Science Letters*,  
880 v. 125, p. 119–128.
- 881 Murton, B.J., Redbourn, L.J., German, C.R., and Baker, E.T., 1999, Sources and fluxes of  
882 hydrothermal heat, chemicals and biology within a segment of the Mid-Atlantic  
883 Ridge: *Earth and Planetary Science Letters*, v. 171, p. 301–317.

- 884 Olafsson, J., Honjo, S., Thors, K., Stefansson, U., Jones, R.R., and Ballard, R.D., 1989, Initial  
885 observations, bathymetry and photography of a geothermal site on the Kolbeinsey  
886 Ridge, *in* *Oceanography 1988 : JOA Mexico* 88, p. 121–127.
- 887 Ondreas, H., Cannat, M., Fouquet, Y., Normand, A., Sarradin, P.M., and Sarrazin, J., 2009,  
888 Recent volcanic events and the distribution of hydrothermal venting at the Lucky  
889 Strike hydrothermal field, Mid-Atlantic Ridge: *GEOCHEMISTRY GEOPHYSICS*  
890 *GEOSYSTEMS*, v. 10, doi: 10.1029/2008GC002171.
- 891 Ondreas, H., Cannat, M., Fouquet, Y., Normand, A., Sarradin, P.-M., and Sarrazin, J., 2009,  
892 Recent volcanic events and the distribution of hydrothermal venting at the Lucky  
893 Strike hydrothermal field, Mid-Atlantic Ridge: *Geochemistry, Geophysics,*  
894 *Geosystems*, v. 10, no. 2, p. Q02006, doi:10.1029/2008GC002171.
- 895 Ondreas, H., Fouquet, Y., Voisset, M., and Radford-Knoery, J., 1997, Detailed study of  
896 three contiguous segments of the Mid-Atlantic Ridge, South of the Azores (37°N to  
897 38°30'N), using acoustic imaging coupled with submersible observations: *Marine*  
898 *Geophysical Researches*, v. 19, p. 231–255.
- 899 Pedersen, R.B., Thorseth, I.H., Nygård, T.E., Lilley, M., and Kelley, D.S., 2010,  
900 Hydrothermal Activity at the Arctic Mid-Ocean Ridges, *in* Rona, P., Devey, C.W.,  
901 Dymont, J., and Murton, B. eds., *Diversity of Hydrothermal Systems on Slow*  
902 *Spreading Ocean Ridges*, p. 67–89.
- 903 Prados, R., Garcia, R., Gracias, N., Escartín, J., and Neumann, L., 2012, A novel blending  
904 technique for underwater gigamosaicing: *IEEE Journal of Oceanic Engineering*, v.  
905 37, no. 4, p. 10.1109/JOE.2012.2204152.
- 906 Scheirer, D.S., Fornari, D.J., Humphris, S.E., and Lerner, S., 2000, High-resolution seafloor  
907 mapping using the DSL-120 sonar system: Quantitative assessment of sidescan and  
908 phase-bathymetry data from the Lucky Strike segment of the Mid-Atlantic Ridge:  
909 *Marine Geophysical Researches*, v. 21, p. 121–142.
- 910 Seher, T., Crawford, W.C., Singh, S.C., and Cannat, M., 2010, Seismic layer 2A variations in  
911 the Lucky Strike segment at the Mid-Atlantic Ridge from reflection measurements:  
912 *Journal of Geophysical Research*, v. 115, p. B07107, doi:10.1029/2009JB006783.
- 913 Singh, S.C., Crawford, W.C., Carton, H., Seher, T., Combier, V., Cannat, M., Canales, J.P.,  
914 Düsünür, D., Escartín, J., and Miranda, J., 2006, Discovery of a magma chamber and  
915 faults beneath a Mid-Atlantic Ridge hydrothermal field: *Nature*, v. 442, p. 1029–  
916 1032.
- 917 Smith, D.K., and Cann, J.R., 1990, Hundreds of small volcanoes on the median valley floor  
918 of the Mid-Atlantic Ridge: *Nature*, v. 344, p. 427–431.
- 919 Smith, D.K., Cann, J.R., and Escartín, J., 2006, Widespread active detachment faulting and  
920 core complex formation near 13°N on the Mid-Atlantic Ridge: *Nature*, v. 443, p.  
921 440–444, doi:10.1038/04950.
- 922 Thurnherr, A.M., Reverdin, G., Bouruet-Aubertot, P., St. Laurent, L.C., Vangriesheim, A.,  
923 and Ballu, V., 2008, Hydrography and flow in the Lucky Strike segment of the Mid-  
924 Atlantic Ridge: *Journal of Marine Research*, v. 66, p. 347–372.

925 Wilson, C., Charlou, J.-L., Ludford, E., Klinkhammer, G., Chin, C., Bougault, H., German, C.,  
926 Speer, K., and Palmer, M., 1996, Hydrothermal anomalies in the Lucky Strike  
927 segment on the Mid-Atlantic Ridge (37°17'N): Earth and Planetary Science Letters,  
928 v. 142, p. 467–477.

929 Yeo, I., Searle, R.C., Achenbach, K.L., Le Bas, T.P., and Murton, B.J., 2011, Eruptive  
930 hummocks: Building blocks of the upper ocean crust: *Geology*, v. 40, no. 1, p. 91–94,  
931 doi: 10.1130/G31892.1.

932